Nucleolar dynamics are determined by the ordered assembly of the ribosome

Jessica Sheu-Gruttadauria[1,2,†], Xiaowei Yan[1,3], Nico Stuurman[1,4], Ronald D. Vale[1,5,†], Stephen N. Floor[2,6 †]

[1] Department of Cellular and Molecular Pharmacology, University of California, San Francisco, San Francisco, CA, USA.
[2] Department of Cell and Tissue Biology, University of California, San Francisco, CA, USA
[3] Present address: Department of Dermatology, Stanford, CA, USA.
[4] Present address: Altos Labs, Redwood City, CA, USA.
[5] Janelia Research Campus, Howard Hughes Medical Institute, Ashburn, VA, USA.
[6] Helen Diller Family Comprehensive Cancer Center, University of California, San Francisco, CA, USA.

[†] Address correspondence to: JS-G jsheugrutt@gmail.com, SNF stephen@floorlab.org, RDV valer@hhmi.org

Abstract (150)

Ribosome biogenesis occurs in the nucleolus, a nuclear biomolecular condensate that exhibits dynamic biophysical properties thought to be important for function. However, the relationship between ribosome assembly and nucleolar dynamics is incompletely understood. Here, we present a platform for high-throughput fluorescence recovery after photobleaching (HiT-FRAP), which we use to screen hundreds of genes for their impact on dynamics of the nucleolar scaffold nucleophosmin (NPM1). We find that scaffold dynamics and nucleolar morphology respond to disruptions in key stages of ribosome biogenesis. Accumulation of early ribosomal intermediates leads to nucleolar rigidification while late intermediates lead to increased fluidity. We map these biophysical changes to specific ribosomal intermediates and their affinity for NPM1. We also discover that disrupting mRNA processing impacts nucleolar dynamics and ribosome biogenesis. This work mechanistically ties ribosome assembly to the biophysical features of the nucleolus and enables study of how dynamics relate to function across other biomolecular condensates.

Highlights

- High-Throughput Fluorescence Recovery After Photobleaching (HiT-FRAP) platform discovers factors that govern macromolecular dynamics of the nucleolar scaffold NPM1
- NPM1 dynamics and nucleolar morphology are determined by specific ribosomal intermediates in the nucleolus
- Mutation of interfaces in NPM1 that mediate ribosome interactions tunes nucleolar dynamics
- Disruption of mRNA processing pathways leads to accumulation of early rRNA precursors in the nucleolus and rigidification

Introduction

Biomolecular condensates are membraneless organelles that are broadly implicated in many cellular processes, including nearly every step in the life cycle of an RNA[1–4]. Over the last decade, increasing evidence suggests that many condensates form through biological phase transitions, driven by multivalent interaction networks formed between nucleic acids and intrinsically disordered regions (IDRs) in protein constituents[5]. These interaction networks imbue condensates with an array of dynamic biophysical properties, including exchange with the environment, internal mixing, viscosity, and surface tension, resulting in material properties that range from liquid to solid-like. It is thought that these biophysical properties influence the biological function of condensates, as pathological mutations that disrupt phase transitions or promote aggregation are associated with disease[1,4]. Emerging work has begun to uncover the molecular principles that underlie condensate dynamics in reconstituted phase separating systems[6–9]. However, mechanistically connecting these features to condensate function in living systems has remained exceptionally challenging.

One of the first identified and largest biomolecular condensates in the cell is the nucleolus, whose main function is coordinating ribosome biogenesis, a process essential for cell viability, growth, and proliferation[10–12]. Decades of genetic, biochemical, and structural studies, primarily in yeast, have provided detailed molecular insight into ribosome assembly[13]. In humans, where this process is largely conserved[14], ribosome biogenesis begins with transcription of the 47S pre-ribosomal RNA (rRNA) by RNA polymerase I, which is processed to yield the small subunit (SSU) associated 18S rRNA and large subunit (LSU) 28S and 5.8S rRNAs (Fig. S1A). The LSU also contains the 5S rRNA, which is transcribed separately by RNA Pol III. This rRNA scaffold undergoes modification, processing, and folding, concomitant with recruitment of 80 ribosomal proteins, all of which is orchestrated by over 200 assembly factors[13,15]. In total, the SSU and LSU proceed through over a dozen discrete intermediates[13,16,17]. Many of these intermediates have been structurally characterized from purified ribosome precursors[16,17], providing a detailed molecular model for stages of ribosome assembly.

In contrast to this precise understanding of ribosome biogenesis, the molecular underpinnings of nucleolar form and how they relate to ribosome assembly are less well understood. On the mesoscale, the nucleolus is composed of three concentric layers enriched for factors involved in sequential steps of ribosome assembly: the fibrillar center (FC) where Pol I transcription occurs, the dense fibrillar component (DFC) where SSU assembly and rRNA processing factors localize, and the granular component (GC) that houses factors involved in maturation of the pre-SSU and assembly of the pre-LSU[18–20] (Fig. S1A). These layers are thought to form through phase separation, driven by multivalent interactions between nucleolar scaffolding proteins, rRNA, and IDRs on ribosomal proteins and assembly factors[19,21–23]. Nucleolar assembly through phase separation leads to several biophysical properties that have been proposed to facilitate ribosome biogenesis. Firstly, it is thought that the three nucleolar layers are immiscible subphases kept distinct by differences in their surface tensions and viscosities, thereby spatially organizing ribosome biogenesis in an assembly line[22,24,25]. The interfaces of these subphases

may be important for molecular hand-off between stages of assembly[26]. Moreover, in vitro and bioinformatic work suggests that the interaction valency of pre-ribosomes with nucleolar scaffolds decreases during maturation through folding and processing of the rRNA, binding of ribosomal proteins, and departure of assembly factors[21,27], promoting the thermodynamic release of mature subunits. Lastly, nucleolar material properties, often described as liquid-like, are thought to be essential for proper ribosome biogenesis. Consistent with this idea, optogenetic clustering of nucleolar scaffolds leads to rigidification and perturbed rRNA processing[28]. Moreover, nucleolar morphology is often disrupted in cancer, aging, and neurodegeneration[29–31].

Together, these observations support a compelling hypothesis that nucleolar condensation is intrinsically coupled with its function in ribosome assembly. However, much of this evidence has come from in vitro reconstitution of a subset of nucleolar constituents. Therefore, the cellular and molecular mechanisms that underlie the biophysical properties of the nucleolus remain poorly defined, which limits our ability to connect nucleolar form to function. This gap arises in large part from limited tools for systematically characterizing the dynamics of biomolecular condensates in living systems.

Here, we introduce a platform to systematically measure dynamics in biomolecular condensates in live cells. The most readily measurable biophysical property of condensates in living systems is macromolecular diffusivity, which is typically assessed using fluorescence recovery after photobleaching, or FRAP[32]. FRAP is a robust and quantitative technique that is widely accessible using commercial microscopes. However, it is also a low-throughput and largely manual technique. To overcome this limitation, we developed a method for High-Throughput Fluorescence Recovery After Photobleaching, which we call HiT-FRAP. This strategy allows FRAP to be used as a readout in arrayed genetic screens, enabling discovery of factors that influence condensate dynamics.

We apply HiT-FRAP to screen hundreds of genes for their impact on the dynamics of a key nucleolar scaffolding protein, nucleophosmin (NPM1). When combined with analysis of nucleolar morphology, we identify four distinct nucleolar phenotypes that are associated with specific stages in ribosome assembly. In addition, we discover a fifth nucleolar phenotype that results from disruption of messenger RNA (mRNA) processing pathways. Characterizing ribosome biogenesis in each of these nucleolar biophysical states reveals that they correspond to changes in the pre-ribosome composition within the nucleolus. Accumulation of early ribosomal intermediates is associated with decreases in NPM1 dynamics, while accumulation of late intermediates leads to increased NPM1 exchange. These trends correlate directly with the partitioning of NPM1 into the nucleolus, which suggests that dynamics are determined by the valency of interactions between pre-ribosome intermediates and nucleolar scaffolds. We further demonstrate that mutation of key interfaces in NPM1 can tune *trans* interactions with ribosomal precursors, which in turn impacts both its partitioning into the nucleolar condensate as well as its macromolecular diffusivity. Together, these results support a model where the assembly state of ribosomal precursors determine the dynamic properties of the nucleolus, providing a direct tie between ribosome biogenesis and nucleolar material properties.

Results

HiT-FRAP: A platform for performing scalable automated FRAP

To identify factors that guide macromolecular dynamics in biomolecular condensates, we developed a platform to perform scalable, fully automated FRAP experiments called HiT-FRAP (Fig. 1A). This pipeline uses data-adaptive imaging strategies to identify automatically and bleach fluorescently labeled organelles in living cells and acquire movies to measure fluorescence recovery (Fig. 1B), eliminating the need for manual designation of regions of interest and increasing experimental throughput by several orders of magnitude. We also developed an automated analysis pipeline that quantifies fluorescence recovery for all bleach points across all acquired positions. We fit recovery data to a simple exponential to prevent over-fitting and export parameters that describe dynamics ($t_{1/2}$ and mobile fraction, which represent time to 50% recovery and percentage of mobile molecules, respectively).

We then applied HiT-FRAP to interrogate dynamics in the largest nucleolar subcompartment, the GC. We focused on the scaffolding protein NPM1, which is thought to contribute directly to GC condensation and is one of the most abundant nucleolar proteins[1]. We appended mNeonGreen to the C-terminus of endogenous NPM1and isolated a clone with homozygous incorporation of the tag to monitor dynamics of all NPM1 molecules. However, we found that this strategy led to decreases in overall expression levels (Fig. S1B). Therefore, to account for both expression level and tag-specific effects, we also generated a cell line where we inserted a C-terminal mScarlet into a single allele, which shows comparable total NPM1 expression levels to unedited cells (Fig. S1B). Both strategies show similar NPM1 localization patterns and FRAP recoveries (Fig. S1C) that reflect published values[33] ($t_{1/2}$ ~2 seconds, Fig. S1C), suggesting that recoveries are not substantially impacted by expression levels or choice of tag.

To validate HiT-FRAP, we measured relative differences in NPM1 dynamics using perturbations previously reported to impact exchange by FRAP. Firstly, we rapidly depleted ATP with 2-deoxyglucose (2-DG) and sodium azide to block both glycolysis and oxidative phosphorylation, which had been previously shown to decrease NPM1 mobility[25]. Similarly, we found that NPM1 exhibited slower recovery (~1.5-fold) and a lower percentage of mobile molecules (~2-fold) as compared to vehicle alone (Fig. 1C). In addition, previous reports have shown that inhibition of the proteasome disrupts nucleolar assembly features, in keeping with its proposed role in proteostasis[34–37]. Consistent with these observations, we found that exposure to the proteasomal inhibitor MG132 decreased NPM1 mobility by ~1.4-fold (Fig. 1D). Lastly, recent work has demonstrated that cellular stress can lead to rigidification of the nucleolus[38]. Therefore, we treated our cells with sodium arsenite and found a ~1.3 fold decrease in mobile fraction (Fig. 1D), consistent with reported values. Together, these results demonstrate that HiT-FRAP enables automated FRAP measurements that can robustly quantify changes in nucleolar dynamics upon perturbation.

Systematic identification of factors that impact NPM1 dynamics

We then applied HiT-FRAP to systematically identify factors that impact NPM1 dynamics in the nucleolus. We focused initially on RNA helicases, which have been proposed to be general regulators of condensate dynamics by modulating RNA interactions that drive phase separation[39–41]. Many RNA helicases also localize to the nucleolus, where they are thought to coordinate multiple steps in ribosome biogenesis[42]. Therefore, we depleted 65 RNA helicases and 9 pairs of phylogenetically related helicases that may act redundantly (Fig. S2A) using an arrayed siRNA library with pools of four siRNAs per target in our mNeonGreen-tagged cell line and monitored NPM1 dynamics using HiT-FRAP.

In total, we identified 13 RNA helicases or helicase pairs whose depletion significantly impacted $t_{1/2}$ and 9 helicases or pairs that showed significant changes in mobile fraction (Fig. 2A and Fig. S2B), totaling 15 unique helicases or helicase pairs that impact NPM1 dynamics. We validated observed phenotypes using individual siRNAs from the pools and confirmed knockdown by western blot for select significant hits (Fig. S2C and D). We also repeated the screen in the mScarlet cell line and replicated most of the identified hits (~80% using same confidence cut-off, Fig. S2E). However, we noted that mobile fraction was less reproducible for both cell lines (Fig. S2B and E), and therefore focused further analysis on those factors that impact kinetics.

8 out of the 13 helicases that influence $t_{1/2}$ localize to the nucleolus or are implicated in ribosome biogenesis (Fig. 2A). Of these helicases, those that led to faster recovery (DDX18[43], DDX54[44], DDX55[45]) are involved in LSU assembly. Conversely, 3 out of 4 nucleolar helicases that led to slower exchange are thought to coordinate early rRNA processing via the SSU processome (DDX41[46], eIF4A3[47] and IGHMBP2[48]). The notable exception was co-depletion of DDX5 and DDX17, which remodel the LSU 28S rRNA[49]. However, these and other “slow” hits (AQR, DHX8, DHX38, eIF4A1+eIF4A2, and UPF1) also participate in other RNA processing pathways, including pre-mRNA processing, nonsense mediated decay (NMD), and translation[50], which could contribute to the phenotype we observe.

Therefore, to better understand how the RNA helicases we identified are impacting NPM1 dynamics, we designed a secondary screen comprised of 290 additional gene depletions (Fig. 2B). 51% of the secondary library targeted ribosomal proteins and select assembly factors. The remainder of the library was composed of STRING-database[51] interactors for the helicase hits, targeting RNA processing pathways including pre-mRNA splicing, transport, translation, and degradation. From this secondary screen, we identified 55 “slow” and 21 “fast” hits that led to significant increases and decreases in $t_{1/2}$, respectively (Fig. 2C). In keeping with the initial RNA helicase hits, functional analysis showed that “fast” hits were enriched for LSU-associated assembly factors and ribosomal proteins (Fig. 2D), which suggests that increased NPM1 exchange results from broad disruption of LSU maturation. Conversely, slow hits were enriched for pathways outside of ribosome biogenesis, including mRNA splicing, processing, and NMD (Fig. 2D). These results suggest that depletion of DDX5+DDX17, DDX41, eIF4A3, and IGHMBP2 may impact nucleolar dynamics through their non-ribosome biogenesis roles, likely downstream of pathway inhibition.

Phenotypic clustering of NPM1 dynamics and morphological features couples nucleolar biophysical state to co-functional gene groups

Perturbations impacting NPM1 dynamics also exhibited notable changes in nucleolar morphology (Fig. 2A and C). Therefore, we expanded our analysis to include morphological descriptors (mean intensity, area, circularity, eccentricity, see Methods) alongside our dynamic measures ($t_{1/2}$, mobile fraction, Fig. 3A). To minimize false positives and plate-to-plate batch effects, we calculated a phenotype score for each of these features that incorporated both the statistical significance and effect size between gene-depleted versus a subset of control (NT) samples from the same plate (see Methods). We then visualized these features together by performing dimensionality reduction through principal component analysis (PCA, Fig. 3A-C, Fig. S3A). Hits were defined by distance from the NT cluster (top 15% cutoff) and similarity in PCA space in at least two out of three biological replicates (Fig. S3B). Results were reproducible across biological replicates and differentially tagged cell lines (Fig. S3B and C).

We then categorized gene hits by their function. Notably, genes that share related functions were adjacent in phenotypic PCA space, separating into five clusters with similar characteristics, which we term nucleolar biophysical states, associated with related gene groups (Fig. 3C and D, Fig. S4A). We validated these groupings by performing hierarchical clustering analysis using phenotypic z-scores, which identified similar gene clusters (Fig. S4B, see Methods). To confirm gene depletion, we performed qPCR for major representative hits in each phenotypic group (Fig. S4C). Four out of five of these states were associated with genes involved in ribosome biogenesis: early processing and rRNA transcription factors (Fig. 3D, “Early”), the RNA exosome that coordinates rRNA end-processing throughout biogenesis (Fig. 3D, “RNA Exosome”), and two groups involved in early and late stages of LSU assembly (Fig. 3D, “LSU1” and “LSU2”). The fifth cluster, however, contained factors with no known role in ribosome biogenesis (Fig. 3D, “Other”) and included most of the “slow” hits identified by HiT-FRAP.

Inhibition of rRNA transcription or the RNA exosome leads to nucleolar fragmentation

We identified a small phenotypic cluster composed of genes involved in rRNA transcription, including PolR1a and the t-UTPs HEATR1, UTP15, and WDR43 (Fig. 3C and D). Depletion of these factors led to nucleolar fragmentation, rounding, and a decrease in dynamics (Fig. 3D and S4B), which aligns with recent reports that Pol I inhibition leads to slowed NPM1 exchange[52]. However, we note that the size of the nucleolus in this cluster approaches the size of the bleach point, and therefore, we are reporting primarily on exchange with the nucleoplasm as opposed to internal rearrangements, confounding direct comparison with other hits in the screen.

Our findings confirm previous reports that nucleolar size correlates with rRNA transcription[53]. Indeed, treating cells with the selective Pol I inhibitors Actinomycin D (ActD, specifically at low doses of 0.04 μg/mL)[54,55] and 500 nM CX5461[56] fully recapitulated the Early phenotypic cluster (Fig. 4A, Fig. S5A). Because NPM1 phase separation is thought to be driven by interactions with assembling ribosomes, we hypothesized that nucleolar shrinking upon transcription inhibition may result from depletion of ribosomal intermediates. We quantified levels of nucleolar rRNA

precursors with RNA FISH using probes against pre-rRNA interspacer regions: the 5′ETS, ITS1, and ITS2, which are processed in early/SSU, SSU, and LSU-associated maturation stages, respectively. As expected, we find that after 2 hours of exposure to low-dose ActD, all rRNA precursors were depleted from the nucleolus, which supports the finding that pre-ribosome intermediates help maintain nucleolar architecture (Fig. 4B).

We also identified a similar but distinct phenotypic cluster containing core components of the RNA exosome, which shows more modest nucleolar shrinking and more irregular shape features than the Early group (Fig. 3C and D, S4B). The RNA exosome coordinates 3′-5′ trimming of rRNA intermediates throughout ribosome biogenesis. However, we found that early rRNA processing factors in the 5′ETS particle, including UTPB (DDX21, PWP2, WDR3, WDR36) and Sof1-UTP7 (WDR46) components, are also enriched in this cluster, which suggests that the observed phenotype may result from exosome processing in early stages of ribosome assembly.

Notably, early rRNA processing steps are coupled with rRNA transcription[57]. We therefore asked whether the fragmentation we observe may result from transcription inhibition and depletion of nucleolar rRNA intermediates as seen in the Early/Pol I cluster. Consistent with this idea, we found that knockdown of the core RNA helicase of the exosome, SKIV2L2, led to a modest but significant depletion of all rRNA precursors from the nucleolus (Fig. 4B). However, this effect was far less substantial than we observed with Pol I inhibition, which suggests that transcription may not be fully ablated. To explore this idea, we performed two-color imaging using a cell line where we endogenously labeled the DFC component Fibrillarin (FBL) alongside NPM1. Upon rRNA transcription shutoff, the concentric nature of the nucleolus disassembles, with the DFC demixing from the GC to form nucleolar caps[58]. We found that nucleolar caps robustly formed upon inhibition of Pol I, while the DFC remained largely internalized within the GC upon SKIV2L2 knockdown (Fig. S5B). These observations suggest that rRNA transcription is still active and may explain the more irregular shape features we observe, in keeping with recent reports that active transcription dictates the shape of the nucleolus and contributes to asphericity[59]. Together, these results indicate that nucleolar fragmentation results from depletion of nucleolar ribosome intermediates, likely downstream of transcription inhibition.

Disruption of key stages in late LSU maturation leads to distinct nucleolar phenotypes

In keeping with GC's primary role in LSU assembly, we identified a large group of genes involved in LSU maturation. A similar phenotype has been reported upon depletion of LSU ribosomal proteins[31]. However, in contrast to these reports, we were able to identify two similar but distinguishable phenotypic groups (LSU1 and 2). Both groups exhibit an increase in nucleolar size, but LSU2 shows a more irregular shape and a substantial decrease in intensity and $t_{1/2}$ (Fig. 3C and D). Consistent with the previously reported LSU phenotype, factors in both LSU clusters are primarily located around the subunit interface, L1 stalk, and the binding site for the central protuberance (CP), corresponding to late-forming LSU landmarks (Fig. S6A). However, recent structural elucidation of human LSU assembly allows us to further map these factors onto discrete LSU intermediates, States A-H[16]. Strikingly, LSU1 is enriched for factors that associate during earlier stages of LSU assembly (States A-F), while LSU2 contained factors that bind at

later stages (States G and H, Fig. 4C and S6A). These factors are differentiated by the transition from State F to G, a major irreversible architectural transition where a protein interaction network composed of early assembly factors departs and allows for binding of downstream maturation factors in preparation for nucleolar export[16,60] (Fig. S6A). This transition is mediated by the AAA+ ATPase MDN1[16,61]. Importantly, MDN1 recapitulated the LSU1 phenotype (Fig. 4E, Fig. S6B and C), which supports that the LSU1 and LSU2 clusters are distinguished by the State F to G transition.

In yeast, disrupting late LSU stages leads to the accumulation of abortive intermediates[62,63]. We therefore hypothesized that the differences in phenotype we observe may result from accumulation of different LSU precursors up and downstream of the F to G transition. Therefore, we assessed rRNA intermediate composition in the nucleolus by FISH for strong hits in both the LSU1 and LSU2 clusters (LSU1: NSA2; LSU2: RPF2). For both groups, we observed a significant nucleolar depletion of the 5′ETS and ITS1 and accumulation of ITS2 (Fig. 4D and S6D). On a global level, however, we saw reduction of the mature 28S (Fig. S6E). As ITS2 is processed immediately after nucleolar export, this result is consistent with an LSU assembly stall, resulting in depletion of early ribosomal precursors and accumulation of aberrant LSU precursors in the nucleolus, ultimately leading to a global defect in LSU biogenesis.

We then sought to determine which LSU precursors accumulate in LSU1 and LSU2 by measuring markers for intermediates both up and downstream of the F-G transition (Fig. 4C). For upstream intermediates, we monitored NOP2, a component of the protein interaction network removed by MDN1. This network shares a mutually exclusive binding site with NOG2 and NOP53, which we used as downstream markers of States G and H. When we depleted the LSU1 gene NSA2, we found a strong enrichment for NOP2 (Fig. 4F), which suggests that states upstream of G and H accumulate in the LSU1 phenotypic cluster. We observed a similar accumulation upon depletion of MDN1 (Fig. S6F), as seen previously upon knockdown of the yeast MDN1 ortholog, Rea1[60]. Interestingly, we also observed a modest increase in nucleolar NOG2 upon depletion of both NSA2 and MDN1 (Fig. 4F and S6F). Therefore, it is possible that some of these upstream intermediates can still recruit downstream factors, in keeping with previous studies in yeast that demonstrate NOG2 can associate with earlier intermediates[64]. Conversely, when we depleted the LSU2 factor RPF2, we observed a strong depletion of NOP2 from the nucleolus and enrichment for State G and H markers (Fig. 4F). We confirmed this effect for another LSU2 cluster factor, NOG2 (Fig. S6F). These results suggest that when LSU2 assembly factors are depleted, maturation can proceed through the critical F to G transition, but then stalls with the formation of partially assembled State G and H intermediates that accumulate within the nucleolus.

Perturbation of mRNA processing pathways results in slowed NPM1 dynamics and accumulation of rRNA precursors in the nucleolus

The last phenotypic cluster was composed of factors with no known direct role in ribosome assembly (Fig. 3D, “Other”). Phenotypically, this gene group showed reduced dynamics and increased intensity (Fig. 3D). Genes in this group are involved in diverse mRNA processing

pathways, including NMD, the exon junction complex (EJC), RNA transport, and pre-mRNA splicing, in particular members of the SF3b spliceosome complex (Fig. 5A). To confirm the observed results, we used inhibitors of the two most represented pathways, NMD and pre-mRNA splicing. Treating cells for 24 hours with the small molecule SMG1i, which prevents activation of the core NMD RNA helicase UPF1[65], phenocopied genetic ablation of NMD factors (Fig. 5B and Fig. S7A). Similarly, treating cells with an inhibitor of the SF3b complex pladienolide B[66] (PladB) for 24 hours recapitulated depletion of splicing-associated factors (Fig. 5C and S7B). Together, these observations validate our screen results. However, we note that the NMD-associated phenotype was less robust in the mScarlet cell line (Fig. S2C) and therefore, we chose to focus further characterization on more reproducible hits.

We hypothesized the "Other" phenotypic cluster may result from a defect in nucleolar ribosome assembly. We noted that the "Other" phenotype shared several characteristics with the "Early" and "Exosome" clusters, including a slight decrease in size (Fig. 3D). However, we did not observe nucleolar cap formation upon depletion of two strong "Other" hits: PHF5A, a core component of the SF3b spliceosome complex, and CNOT1, the central scaffold for the CCR4-NOT deadenylase complex whose nuclear roles include mRNA export and RNA surveillance (Fig. S7C), which suggests that rRNA transcription and biogenesis are still active and able to maintain the concentric architecture of the nucleolus. Therefore, we reasoned that additional disruptions to ribosome biogenesis may lead to the observed phenotype. Indeed, upon depletion of either CNOT1 or PHF5A, we observed nucleolar enrichment for ITS1 and 2, and for PHF5A, the 5′ETS (Fig. 5C). This enrichment did not correspond to a global increase in mature rRNAs (Fig. S7D). These results suggest that depletion of the "Other" gene group leads to an accumulation of aberrant, early precursors in the nucleolus, resulting in an overall decrease in ribosome biogenesis.

Changes in NPM1 dynamics are associated with shifts in ribosome intermediate balance in the nucleolus

Our analysis of nucleolar ribosome biogenesis intermediates across the identified phenotypic clusters showed that the balance of nucleolar pre-ribosome intermediates was strongly correlated with NPM1 dynamics. Accumulation of early rRNA intermediates in the "Other" gene group was associated with slower exchange, while depletion of early intermediates and accumulation of very late LSU precursors (States G/H, associated with the LSU2 gene group) accompanied faster exchange. Depletion of all nucleolar rRNA precursors upon RNA Pol I inhibition and perturbation of the RNA exosome led to nucleolar disassembly and fragmentation. Notably, current models in the field suggest that nucleolar condensation is driven by *trans* interactions between NPM1 and surfaces on ribosome intermediates, in particular rRNA and IDRs. The valency of *trans* interactions is thought to decrease as the ribosome matures, ultimately supporting thermodynamic flux of the ribosome out of the nucleolus[21,27]. We therefore hypothesized that the strength of interactions between NPM1 and developing preribosomes determines phase separation as well as macromolecular dynamics. In support of this idea, we observed a strong direct correlation between partitioning behavior and $t_{1/2}$ for select hits across

phenotypic clusters (Fig. 6A, r = 0.87, p = 0.0001), which supports that the mechanisms underlying phase separation may also determine scaffold dynamics.

To further explore the molecular basis for the connection between ribosomal intermediates and NPM1 dynamics, we focused on the two LSU phenotypic clusters we identified, where specific classes of pre-LSU intermediates accumulate (LSU1: State F and LSU2: State G/H, respectively). Importantly, these clusters are also distinguished by both changes in dynamics and partitioning, allowing us to directly correlate these features with potential *trans* interaction interfaces on ribosome intermediates. The protein interaction network removed by MDN1 in the State F to G transition contains numerous IDRs (Figure S8A), leading to a reduction in total IDR length of ~50%. In addition, ~9% of the 28S rRNA undergoes compaction during this transition through the formation of inter-domain rRNA interactions (domains I:V and III:VI, stabilization of portions of expansion segments in domain IV), initial bending of the L1 stalk, and compaction of domain IV helices upon installation of the CP (Fig. S6A and S8A). Together, the substantial decrease in trans interactions between State F and States G/H may lead to a weakened nucleolar condensate, resulting in the decreased partitioning and increased dynamics we observe in LSU2.

NPM1 dynamics and nucleolar partitioning are determined by interactions with developing preribosomes

We next sought to experimentally determine how interactions with preribosomes impacted NPM1 dynamics. NPM1 contains an N-terminal pentamerization domain, an intrinsically disordered linker region, and a C-terminal RNA-binding three-helix bundle (Fig. 6B). While all domains are necessary for phase separation, *trans* interactions with ribosomes are best studied within the intrinsically disordered linker region[22]. In addition, in the presence of crowding agents, homotypic interactions between the IDR in different NPM1 molecules can also drive phase separation[23], although these appear to contribute less strongly to partitioning in cells[21].

We therefore chose to focus on the IDR of NPM1. The IDR exhibits a charged block pattern composed of two acidic, negatively charged regions that alternate with two basic, positively charged regions (Fig. 6B). The two acidic domains A2 and A3 are thought to mediate heterotypic interactions with positively charged linkers in nucleolar proteins while B1 and B2 bind to rRNA[22]. Homotypic interactions are facilitated, in turn, through interactions between A3 and B2[23]. To determine how these domains contribute to NPM1 phase separation and dynamics in cells, we generated lentiviral constructs with mScarlet-tagged NPM1 where we selectively mutated charged domains in the IDR, similar to those used previously in vitro[23,67] (Fig. 6B). We abolished the negative charge of A2 and A3 by replacing them with $(GGS)_4G$ and $(GGS)_9G$ linkers, respectively, which we call $NPM1^{mA2}$ and $NPM1^{mA3}$. For the basic regions B1 and B2, we generated $NPM1^{mB1}$ and $NPM1^{mB2}$, where we mutated all lysines to alanines apart from those within annotated nuclear localization signals.

We then introduced these NPM1 mutant constructs into unedited HeLa cells and measured interactions with developing pre-ribosomes for mutants lacking the largest charged tracks,

NPM1^{mA3} and NPM1^{mB2}. We found that both mutants could still interact with WT NPM1, likely through formation of heteropentamers, although there was a slight decrease in association for NPM1^{mB2} (Fig. S9A). Therefore, to eliminate the contribution of indirect interactions through WT NPM1, we also introduced constructs into HeLa cells where endogenous NPM1 was stably ablated (Fig. S9B). We found that mutation of A3 increased association with markers of pre-LSU intermediates and most rRNA precursors, while loss of B2 led to a modest decrease in association (Fig. 6C and S9C). This effect was strengthened in the absence of WT NPM1. The substantial increase in association with preribosomes upon removal of A3 supports in vitro findings that suggest homotypic inter- or intramolecular binding between A3/B2 may tune the availability of each region for heterotypic interactions, potentially acting as a regulatory switching mechanism[23]. However, these results also strongly suggest that the basic B2 region contributes most substantially to association with assembling preribosomes.

Having established the ability to directly tune NPM1-preribosome interactions, we asked how these mutations impact partitioning and dynamics within the nucleolus. In the presence of endogenous NPM1, we found that NPM1^{mA2} showed a decrease (~30%) in nucleolar partitioning (Fig. 6D), which likely results from loss of interactions with R-rich nucleolar proteins. Similarly, mutating the smaller basic tract in NPM1^{mB1} resulted in a modest decrease (~20%) in partitioning behaviors. Neutralization of the larger A3 tract, however, led to a ~30% increase in partitioning into the nucleolus, while loss of B2 resulted in a ~75% decrease of nucleolar localization. In keeping with our co-immunoprecipitation results, these effects were strengthened in the absence of endogenous NPM1 (Fig. S9D). In fact, NPM1^{mB2} was excluded from the nucleolus and diffuse within the nucleoplasm, supporting its key role in driving phase separation.

Importantly, we found that the dynamics of these mutant constructs were directly correlated to their partitioning behaviors (Fig. 6E). The strongly partitioning construct NPM1^{mA3} showed a ~20% increase in $t_{1/2}$. Conversely, NPM1^{mA2} and NPM1^{mB2}, which partitioned more weakly, exhibited significantly faster recoveries (~20% and 40%, respectively). These findings are consistent with a model where the strength of associations between NPM1 and ribosome intermediates determine both phase separation and macromolecular dynamics (Fig. 7A).

Discussion

Connecting condensate dynamics to biological function is an ongoing challenge in the field. Emerging work using in vitro reconstituted phase separating systems has begun to shed light on the molecular principles underlying condensate dynamics in idealized systems but relating these findings to functional condensates in vivo has been challenging. Here, we have used HiT-FRAP to identify factors that influence condensate dynamics in living cells. We apply this platform to show that dynamics of the nucleolar scaffold NPM1 are sensitive to the ordered assembly of the ribosome, where early ribosomal precursors that participate in high valency *trans* interactions decrease NPM1 diffusional dynamics, while low valency late precursors increase diffusional exchange. These results demonstrate that ribosome assembly directly impacts the biophysical properties of the nucleolus through the dynamics of its main scaffold NPM1.

Insights into nucleolar condensate biophysics and assembly principles

Our results support a physical picture where nucleolar scaffold dynamics are determined by the valency and thermodynamic strength of heterotypic interactions that drive condensate formation, as seen in other network fluids and in vitro reconstituted condensate systems[7,68]. As these interactions change over the course of ribosome maturation, the nucleolus must exhibit non-uniform composition and material features, from rRNA transcription at the nucleolar center to precursor release at its surface. It has recently been demonstrated that the radial movement of rRNA leads to viscoelasticity within the nucleolus, forming a gel-like structure that fluidizes with progressive processing as it reaches the nucleolar periphery[59]. Our results suggest that NPM1 likely exhibits similar spatiotemporal variance built upon this rRNA core.

Importantly, these results indicate the nucleolus does not behave as a simple fluid, as has been proposed from work using NPM1 as a proxy for the liquid-like features of the nucleolus. This finding underscores a key question: how do different nucleolar components contribute to the physical features of the resulting condensate? And how do these dynamics impact condensate function? We anticipate that for the nucleolus, these principles will vary spatially in accordance with ribosome maturation. Given our results and others, we hypothesize that the nucleolar surface most closely represents the liquid-like system represented in current NPM1-based nucleolar reconstitution systems. Therefore, we propose that NPM1 dynamics may most strongly impact late subunit maturation and nucleolar export at this interface, which we discuss further below. Moving forward, systematically mapping how the dynamics of other constituents relate to their function and nucleolar material properties will be essential. We anticipate that HiT-FRAP will enable this endeavor.

Connecting nucleolar assembly principles to ribosome assembly

Consistent with previous results[31,69,70], we find that nucleolar dynamics are sensitive to late stages of LSU assembly. Our work reveals that this sensitivity is specific to two steps, representing the final two stages in nucleolar pre-LSU maturation. The first is the MDN1-mediated removal of a nucleolar protein interaction network comprised of early assembly factors (State F to State G/H)[16]. The second is release of pre-LSUs into the nucleoplasm. We show that disruption of each of these stages leads to nucleolar accumulation of abortive State F and State G/H intermediates, respectively. This accumulation is associated with progressive weakening of the nucleolar condensate, which manifests as an increase in NPM1 diffusion. We therefore propose that the human State G/H intermediates represent the final stages before export, where the transition to State I licenses release by falling below the threshold of valency required for nucleolar sequestration (Fig. 7B and S8B). This transition is hallmarked by installation of the CP coupled with binding of the rixosome, a complex necessary for ITS2 processing. *Trans* interactions may change in several ways during this transition. Several IDRs are lost or stabilized, although in total, IDRs increase due to arrival of rixosome components (Fig. S8B). More notably, domains IV and V of the 28S rRNA mature, collectively resulting in a ~30% decrease in uncompacted rRNA (Fig. S8B). This mechanism appears to be conserved, as recent work in yeast identified a similar LSU intermediate as the final nucleolar assembly stage[63].

However, intriguingly, engineered rRNA that lacked large portions of ITS2 and 28S expansion segments did not globally impact ribosome export, despite being comparable in size to the compaction of the 28S that occurs during the transition to State I[16,71,72]. These findings suggest at least two possibilities: 1) that certain "uncompacted" rRNA regions may not be available for *trans* interactions, or 2) that additional factors outside of these interactions may govern sequestration within the nucleolus. Therefore, further work characterizing export incompetent intermediates will be necessary to understand the structural mechanism for nucleolar release.

Taken together, we propose that the biophysical features and ribosomal intermediates associated with the LSU1 and LSU2 groups represent the outermost molecular "layers" of the nucleolus (Fig. 7B), providing biophysical insight into the nucleolar interface. This idea is supported by recent *in situ* structural efforts in *Chlamydomonas* nucleoli that revealed a gradient of ribosome assembly intermediates at the nucleolar surface[73]. Importantly, interfaces are a unique environment where the condensate and its surroundings meet, and as such, have been shown to form distinct chemical and functional environments in other condensate systems[74–78]. In the case of the nucleolus, the final stages of precursor assembly must interact with the nuclear environment, which could influence these steps in nontrivial ways. Consistent with this idea, it has been shown that disruption of chromatin structure leads to amorphous nucleolar morphology reminiscent of the LSU2 phenotype[59]. It is therefore likely that the nucleolar interface possesses specialized features to facilitate handoff. In support of this hypothesis, recent work has shown that the nucleolar rim is a compositionally distinct compartment, and intriguingly, is enriched for NPM1, factors removed in the State F to G transition (BOP1, DDX18, EBP2, FTSJ3, NOC2L, NOC3L), State G/H factors (NOG2, RPF2, uL18), and factors involved in remodeling of State G/H to I (GNL3, CCDC86)[79]. It will be exciting to consider how the unique environment of the nucleolar interface may facilitate the key molecular events associated with these architectural changes, while remaining distinct from the nuclear surroundings and ensuring only properly assembly ribosomes are released.

Biophysical changes in the nucleolus in response to stress

We also discovered unexpected ties between nucleolar dynamics and diverse mRNA processing pathways. Connecting our observations to reports in the literature suggest that they may relate to the nucleolus's role in cellular stress responses. For example, rRNA processing stalls during acute stress and leads to accumulation of unprocessed precursors, which decrease nucleolar dynamics and are stored until stress is alleviated[38,80]. This response is reminiscent of the pre-mRNA processing phenotype we observe and suggests it may result from induction of cellular stress. In support of this idea, disruption of splicing causes stress granule formation and proteotoxic stress[81,82]. Furthermore, during stress, the nucleolus reversibly stores misfolded proteins whose aggregation is prevented through interactions with scaffolds such as NPM1[34]. This accumulation leads to nucleolar rigidification, similar to the "Other" phenotype. Interestingly, inhibition of NMD induces expression of truncated proteins that aggregate[83] and could enter the nucleolus, leading to the rigidification we observe. Therefore, the "Other" phenotype may be a biophysical signature of nucleolar stress. This finding suggests that nucleolar dynamics may facilitate crosstalk between ribosome biogenesis and cellular homeostasis. This interplay will

likely be important in the context of diseases associated with nucleolar stress[84]. For example, in neurodegeneration, both nucleolar dynamics and many RNA processing pathways are disturbed[67,85,86,86–89]. Thus, this discovery highlights the advantage of our screening approach in connecting condensate function more broadly to other cellular pathways.

Conclusion

In conclusion, our work establishes that NPM1 dynamics are shaped by interactions with ribosome intermediates. This finding implies that these interactions may play important roles in chaperoning assembly, in particular late LSU maturation steps. Future work will be necessary to uncover the role of phase-separating scaffolds and their dynamic behaviors in this assembly process. Moreover, our results support a model where the same molecular interaction networks that drive phase transitions in condensates may also dictate their dynamics. Therefore, dynamics may be tunable by the network connectivity principles recently proposed to broadly underlie the formation of diverse biomolecular condensates[90]. Indeed, diseases that manipulate this network in the nucleolus have been previously shown to impact nucleolar dynamics and disrupt function[34,67,86,91]. This model may also shed light on driving forces for poorly dynamic, pathological inclusions of phase-separating proteins[1], which could arise from shifts in the stoichiometries of interactors. Lastly, we anticipate our observations may apply to other biomolecular condensates, as many are formed through similar networking interactions with a core set of scaffolds. HiT-FRAP now provides a toolset for uncovering the principles that drive dynamics across other biomolecular condensates and, importantly, lays the groundwork for connecting these principles to condensate function in the cell.

Author contributions

Conceptualization, J.S-G.; Investigation, J.S-G.; Writing – Original Draft, J.S-G.; Writing – Review & Editing, J.S-G., S.N.F., R.D.V.; Methodology, J.S-G., X.Y., N.S.; Resources, J.S-G. and R.D.V.; Formal analysis, J.S-G., X.Y., N.S.; Software, J.S-G., X.Y., N.S.; Funding Acquisition, J.S-G., S.N.F., and R.D.V.; Supervision, S.N.F. and R.D.V.

Acknowledgments,

We thank members of the Floor and Vale labs for feedback on this work and their continued support. We additionally thank Dyche Mullins and members of the Mullins lab for their generous support. SMG1i was generously provided by Robert Bridges, Ph.D. of the Rosalind Franklin University of Medicine and Science and Cystic Fibrosis Foundation Chemical Compound Program. JS-G is a Hanna H. Gray Fellow of the Howard Hughes Medical Institute. This work was supported by the National Institutes of Health R35GM149255 (to SNF). SNF is a Pew Scholar in the Biomedical Sciences, supported by The Pew Charitable Trusts. RDV is supported by the Howard Hughes Medical Institute.

Competing interests

None declared.

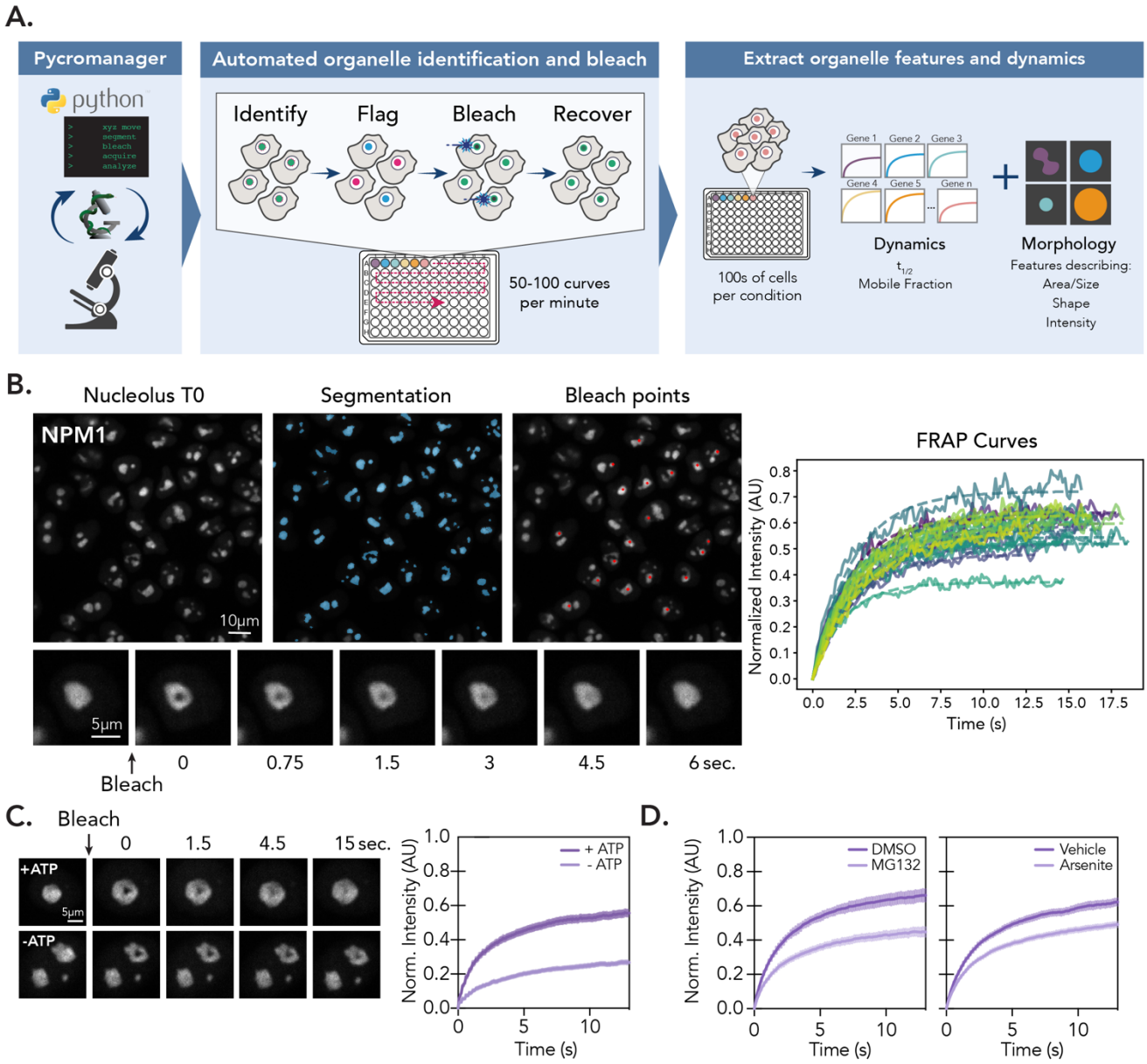

Figure 1: HiT-FRAP: A platform for performing scalable, automated FRAP experiments. (A) Schematic overview of HiT-FRAP pipeline. See also: Methods. (B) Example images show automated FRAP steps. Left, segmentation of fluorescently labeled nucleoli (blue masks, see methods) and bleach point determination (red points). Below, zoom of single nucleolus bleach and recovery time course. Right, normalized FRAP curves generated from a single field of view. Raw intensities shown as solid line, single-exponential curve fit shown as dotted line. (C) NPM1-mNeonGreen cell lines were treated with 10 mM sodium azide and 6 mM 2-deoxyglucose for 10 min to deplete cellular ATP prior to bleaching experiment. Left, images of single nucleolus bleach and recovery time course for vehicle and ATP deplete. Right, FRAP curves (n = 250 nucleoli, error bars are 95% CI). (D) NPM1-mNeonGreen cell lines were treated with 10 μM MG132 for 1 hr (left) or 200 μM sodium arsenite for 1 hr prior to bleaching experiment. (n = 250 nucleoli, error bars are 95% CI).

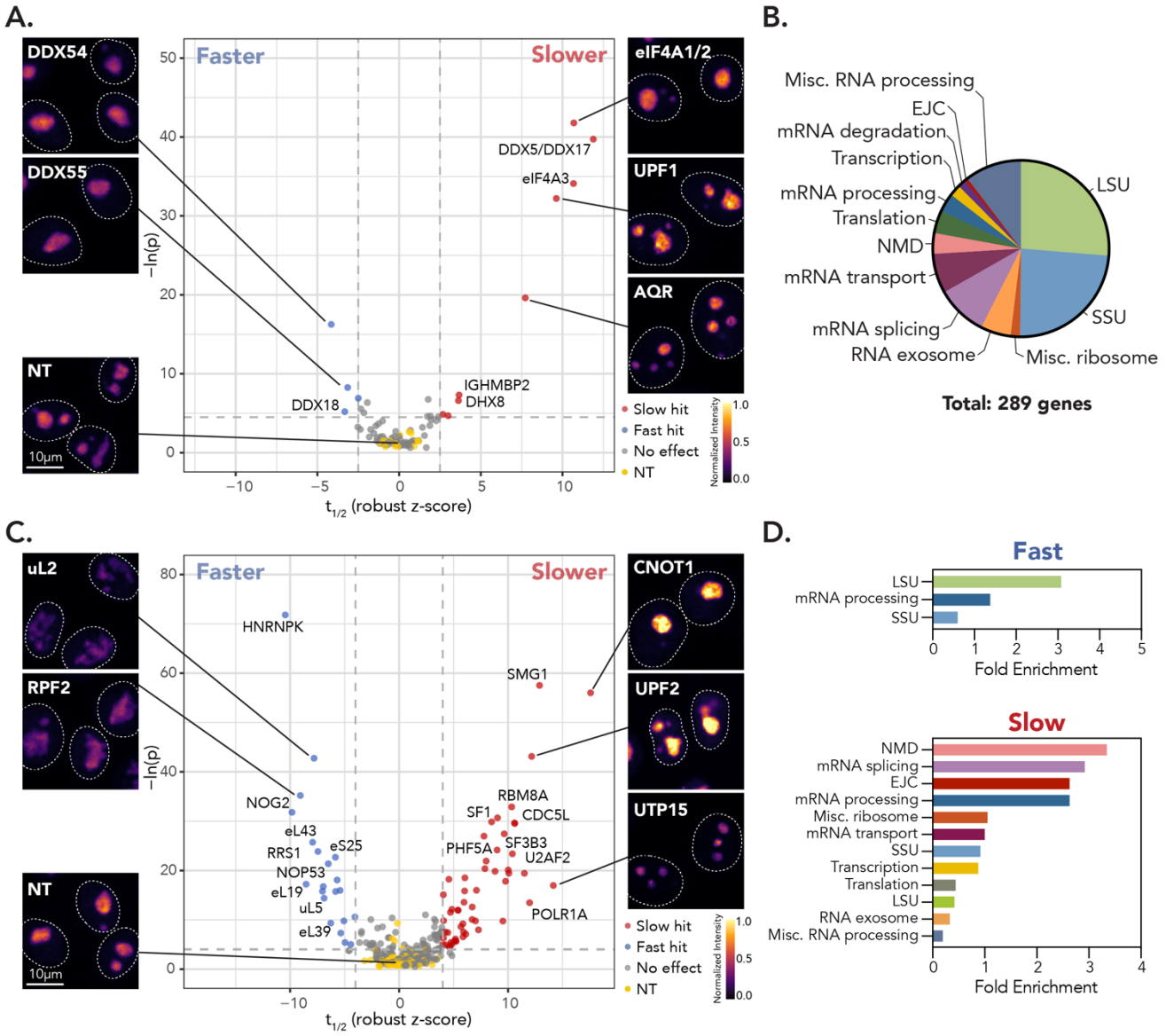

Figure 2: HiT-FRAP identifies RNA helicases and RNA processing factors that impact nucleolar dynamics. (A) Selected images and volcano plot for $t_{1/2}$ for primary RNA helicase screen, highlighting helicase hits that resulted in increased (red, "slower") or decreased (blue, "faster") $t_{1/2}$ relative to non-targeting control cells (yellow; FDR < 0.05 and z-cutoff of ± 2.5 shown as dotted lines, see Methods). Non-significant gene targets shown in gray. x-axis plots robust z-score for $t_{1/2}$ (see Methods). Images are scaled equally and colored linearly with mp-inferno LUT. (B) Functional gene distribution of secondary screen by manual annotation. (C) Selected images and volcano plot as in (A) for secondary screen. (FDR < 0.05 and z-cutoff of ± 4, shown as dotted lines). (D) Gene enrichment for functional groups, determined by manual annotation, for "fast" (smaller $t_{1/2}$) and "slow" (larger $t_{1/2}$) hits.

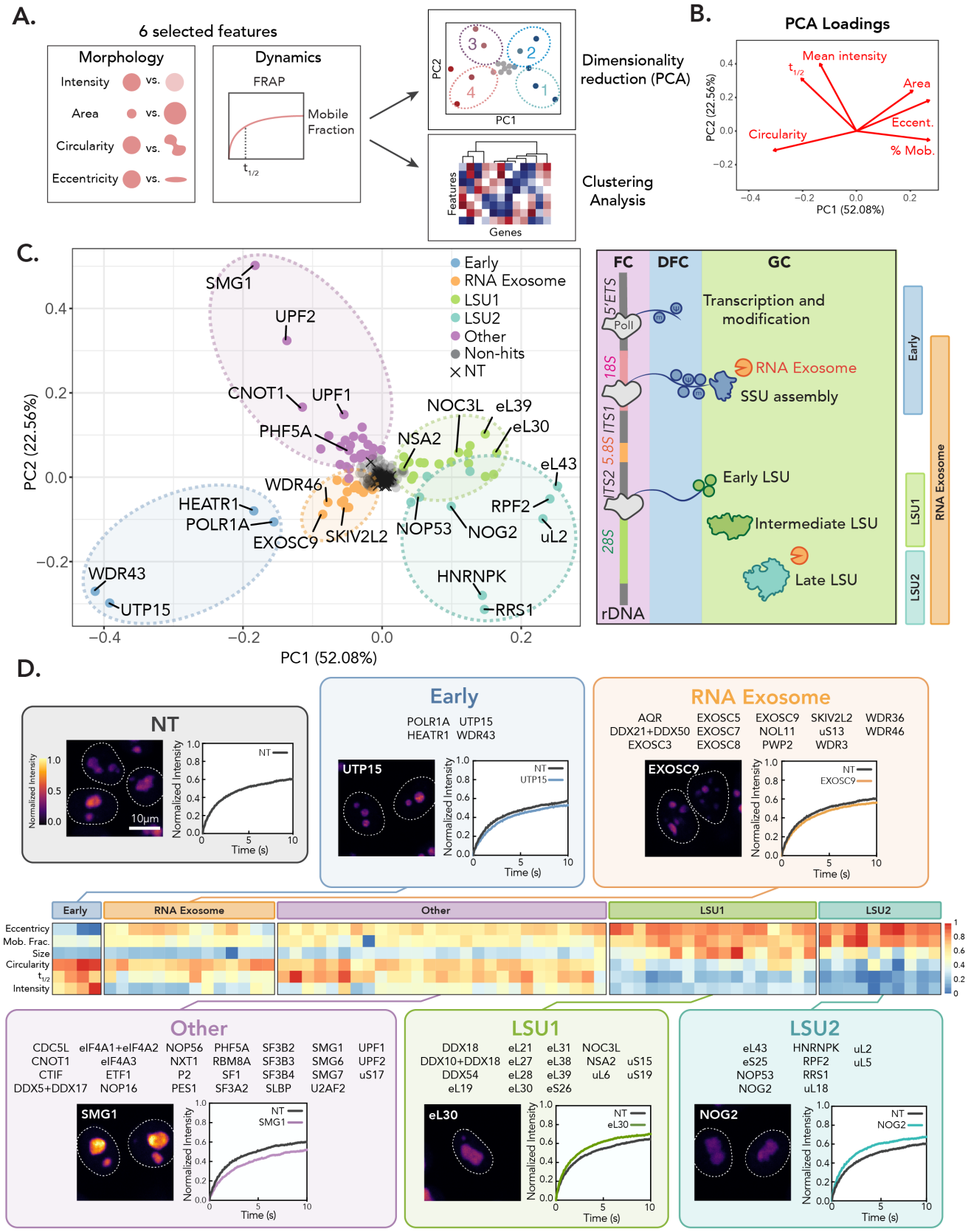
A.
6 selected features
Morphology
Intensity vs.
Area vs.
Circularity vs.
Eccentricity vs.
Dynamics
FRAP
Mobile Fraction
$t_{1/2}$
PC2
PC1
Dimensionality reduction (PCA)
Features
Genes
Clustering Analysis
B.
PCA Loadings
Mean intensity
$t_{1/2}$
Area
Eccent.
% Mob.
Circularity
PC2 (22.56%)
PC1 (52.08%)
C.
Early
RNA Exosome
LSU1
LSU2
Other
Non-hits
NT
SMG1
UPF2
CNOT1
UPF1
PHF5A
NOC3L
eL39
eL30
NSA2
eL43
WDR46
HEATR1
POLR1A
EXOSC9
SKIV2L2
NOP53
NOG2
RPF2
uL2
WDR43
UTP15
HNRNPK
RRS1
PC2 (22.56%)
PC1 (52.08%)
FC
DFC
GC
5'ETS
18S
ITS1
5.8S
ITS2
28S
rDNA
Pol I
Transcription and modification
RNA Exosome
SSU assembly
Early LSU
Intermediate LSU
Late LSU
Early
LSU1
LSU2
RNA Exosome
D.
NT
Normalized Intensity
10μm
Time (s)
Early
POLR1A UTP15
HEATR1 WDR43
UTP15
RNA Exosome
AQR EXOSC5 EXOSC9 SKIV2L2 WDR36
DDX21+DDX50 EXOSC7 NOL11 uS13 WDR46
EXOSC3 EXOSC8 PWP2 WDR3
EXOSC9
Early
RNA Exosome
Other
LSU1
LSU2
Eccentricy
Mob. Frac.
Size
Circularity
$t_{1/2}$
Intensity
Other
CDC5L eIF4A1+eIF4A2 NOP56 PHF5A SF3B2 SMG1 UPF1
CNOT1 eIF4A3 NXT1 RBM8A SF3B3 SMG6 UPF2
CTIF ETF1 P2 SF1 SF3B4 SMG7 uS17
DDX5+DDX17 NOP16 PES1 SF3A2 SLBP U2AF2
SMG1
LSU1
DDX18 eL21 eL31 NOC3L
DDX10+DDX18 eL27 eL38 NSA2 uS15
DDX54 eL28 eL39 uL6 uS19
eL19 eL30 eS26
eL30
LSU2
eL43 HNRNPK uL2
eS25 RPF2 uL5
NOP53 RRS1
NOG2 uL18
NOG2

Figure 3: Phenotype clustering identifies gene groups associated with specific nucleolar signatures. (A) Schematic overview of phenotypic clustering analysis (see also: Methods). (B) PCA loadings for each nucleolar feature. (C) PCA colored by phenotype cluster. Schematic of nucleolar ribosome biogenesis stages shown on right, with phenotypic classes associated with stages indicated. (D) Heatmap showing features as z-scores of PCA clusters. Z-scores were scaled from 0 to 1. Insets show image and representative FRAP curve for select hit in each phenotypic cluster. Images are scaled equally and colored with mpl-inferno LUT to show relative intensity differences. FRAP curve of NT control and gene depletion shown (n = 250 nucleoli, error bars are 95% CI).

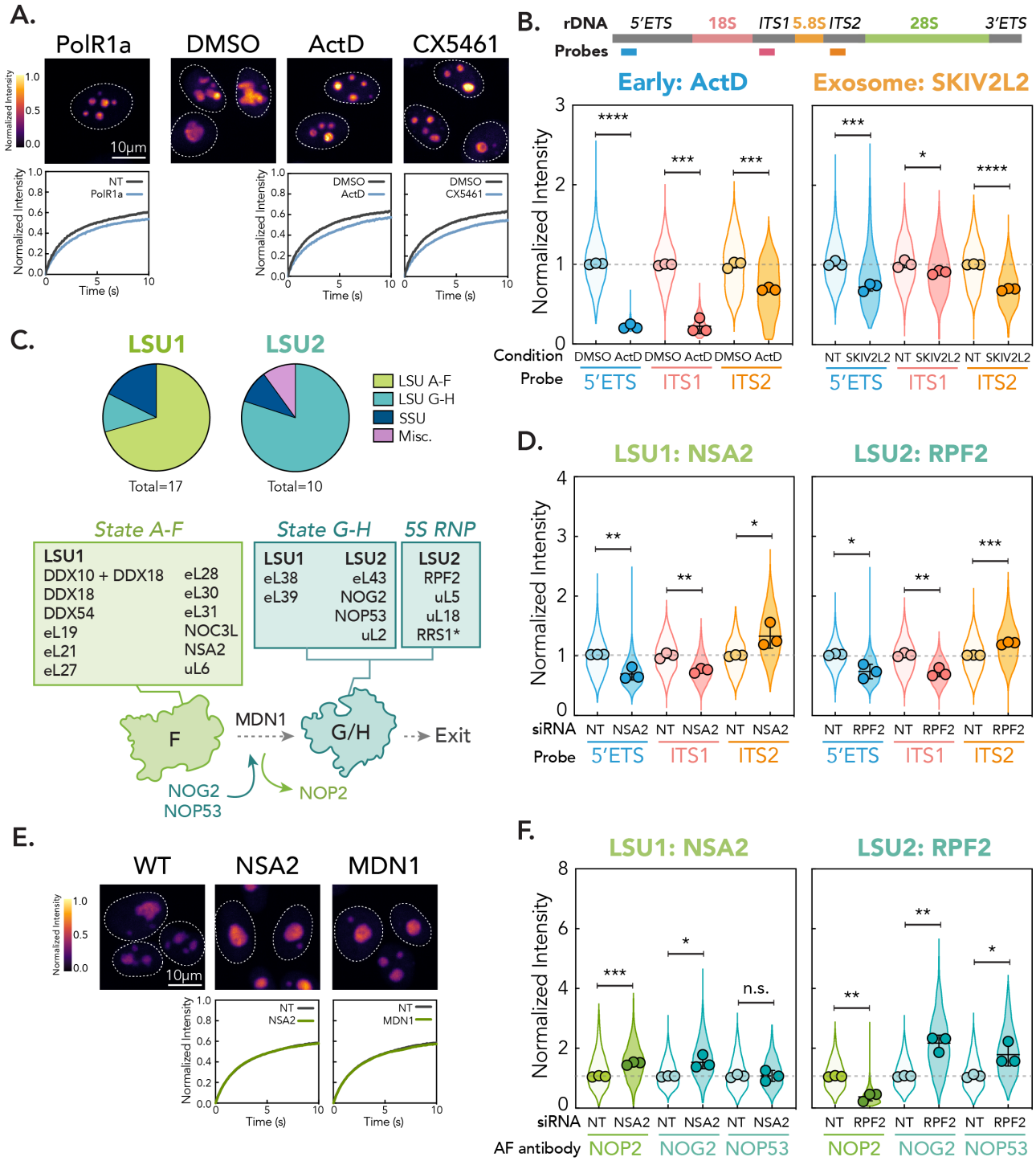

Figure 4: Distinct nucleolar phenotypes are associated with discrete stages in ribosome biogenesis. (A) Comparison between PolR1a knockdown (Early cluster) phenotype and treatment of cells with Pol I inhibitors (0.04 μg/mL ActD and 500 nM CX5461 for 2 hr). Images are scaled equally and colored with mpl-inferno LUT to show relative intensity differences. FRAP curves for NT/vehicle control vs. gene depletion/drug shown (n = 250 nucleoli, error bars are 95% CI). (B) rRNA FISH for Early (ActD) and Exosome cluster (knockdown of SKIV2L2).

Schematic shows position of probes in 47S rRNA. Violin plots show spread of individual data points across three biological replicates (n = 600 nucleoli per replicate, points represent means of replicates, error bars are SD). The dotted line shows non-targeting control level. p-values calculated using two-tailed unpaired t-test between biological replicates. * $p < 0.05$, ** $p<0.01$, *** $p < 0.001$, **** $p<0.0001$. (C) Mapping genes in LSU1 and LSU2 phenotypic clusters onto LSU intermediates and schematic of State F to G transition. * = RRS1 associates in State A-F but is critical in 5S RNP recruitment. (D) rRNA FISH for representative hits in LSU1 (NSA2) and LSU2 (RPF2) gene clusters, as in (B). (E) Comparison of LSU1 cluster hit NSA2 and knockdown of MDN1. Images are scaled equally and colored with mpl-inferno LUT to show relative intensity differences. FRAP curves for NT vs. gene depletion shown (n = 250 nucleoli, error bars are 95% CI). (F) Nucleolar immunofluorescence of LSU intermediate markers for LSU1 and LSU2 representative gene hits. Three biological replicates were performed (n = 600 nucleoli per replicate, spread of individual nucleoli shown as violin, error bars are SD). Dotted line shows non-targeting control level. p-values calculated using two-tailed unpaired t-test between biological replicates. n.s. = not significant, * $p < 0.05$, ** $p<0.01$, *** $p < 0.001$.

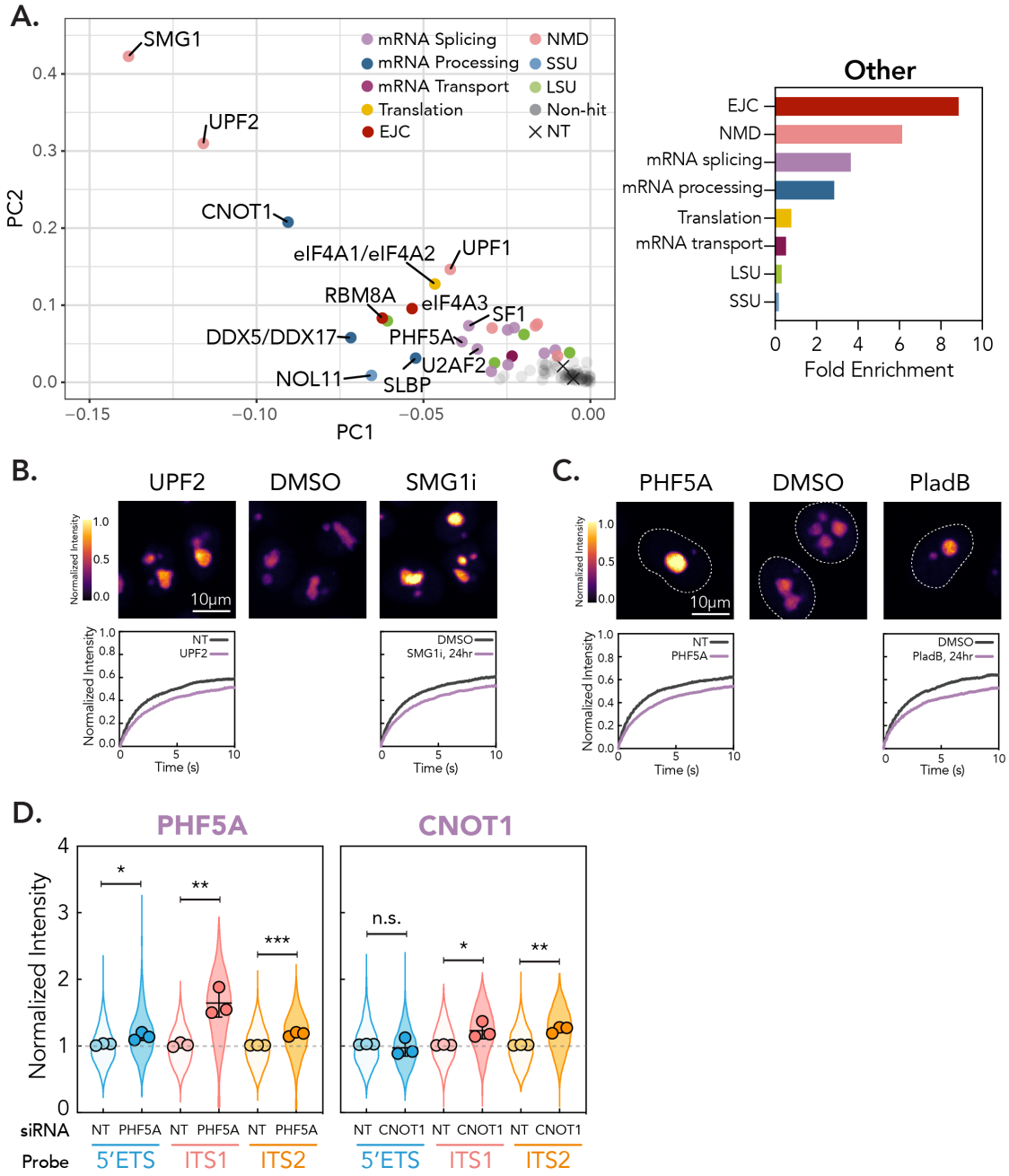

Figure 5: Disruption of mRNA splicing leads to slowed NPM1 dynamics and accumulation of rRNA precursors in the nucleolus. (A) "Other" phenotypic cluster shown as zoom of PCA in Fig. 3C. Fold enrichment for functional groups in "Other" cluster shown on right. (B) Comparison between "Other" hit UPF2 and treatment with NMD inhibitor SMG1i (300 nM for 24 hr). Images are scaled equally and colored with mpl-inferno LUT to show relative intensity differences. FRAP curves for NT/vehicle vs. gene depletion/SMG1i shown (n = 250 nucleoli, error bars are 95% CI). (C) Comparison between "Other" representative hit PHF5A and treatment with splicing inhibitor PladB (10 nM for 24 hr). Images are scaled equally and colored with mpl-inferno LUT to show relative intensity differences. FRAP curves for NT/vehicle vs. gene

depletion/PladB shown (n = 250 nucleoli, error bars are 95% CI). (D) rRNA FISH for representative gene hits in “Other” phenotypic cluster, as in Fig. 4B. n.s. = not significant, * $p < 0.05$, ** $p<0.01$, *** $p < 0.001$.

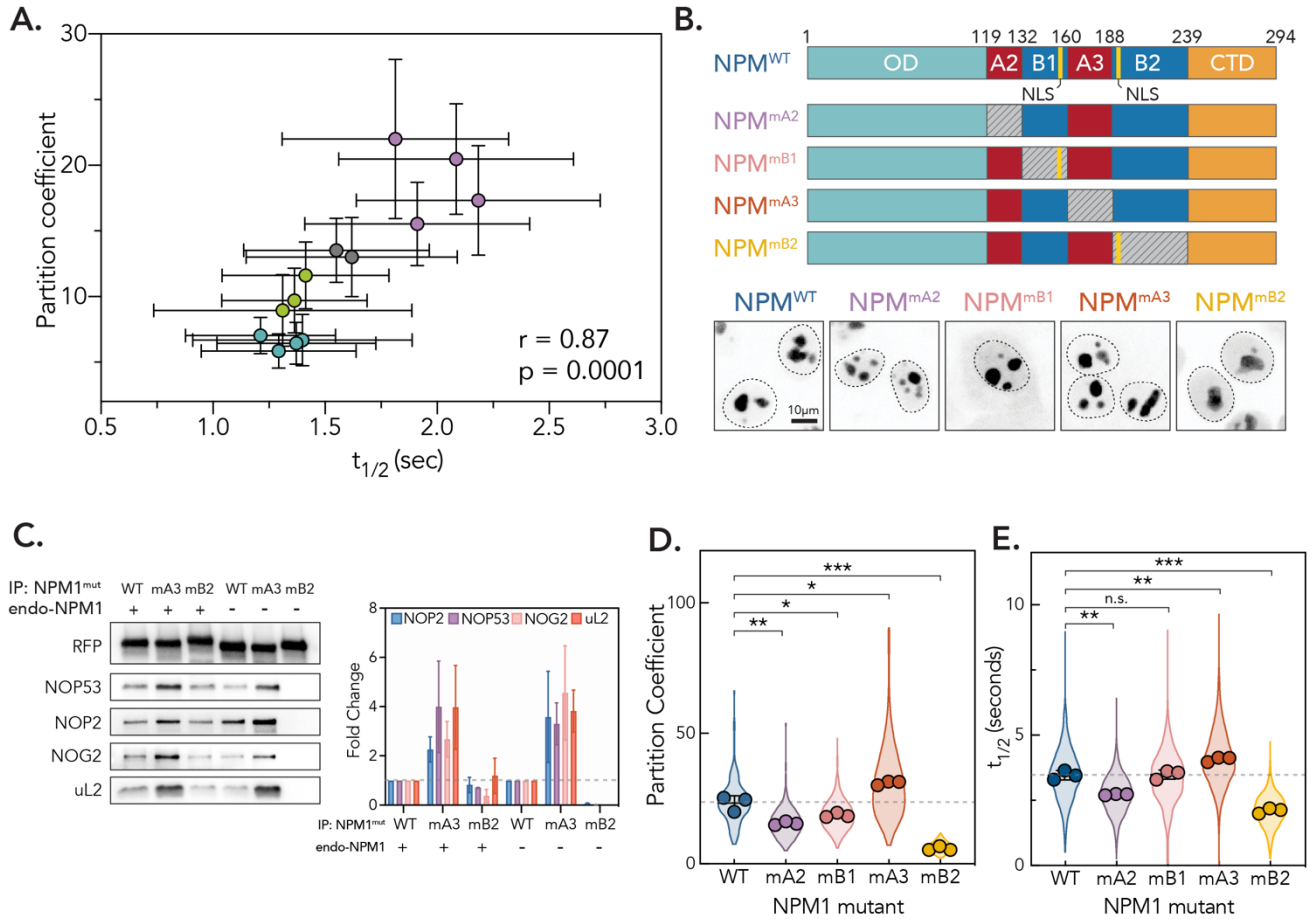

Figure 6: NPM1 dynamics are determined by interactions that drive partitioning into the nucleolus. (A) Partition coefficients vs. $t_{1/2}$ for representative hits in phenotypic clusters (n = 100 nucleoli, points are mean, error bars are SD). Pearson r and p-value indicated. (B) Schematic of NPM1 mutant constructs. Gray box represents charge neutralization. Yellow lines represent annotated nuclear localization signal (NLS). Representative images shown for localization pattern of each mutant construct. (C) Left: representative western blot for ribosome assembly factors and proteins associated with immunoprecipitated NPM1 with indicated mutations. Right: Quantification across replicates. Error bars are SD. n = 3. (D) Partition coefficients for each mutant construct. Violin plot shows spread of individual points for 3 biological replicates (n = 40 nucleoli per replicate, points show means of each replicate, error bars are SD). p-values calculated using two-tailed unpaired t-test between biological replicates. * $p < 0.05$, ** $p<0.01$, *** $p < 0.001$. (E) $t_{1/2}$ for each mutant construct. Violin plot shows spread of individual points for 3 biological replicates (n = 250 nucleoli per replicate, points show means of each replicate, error bars are SD). p-values calculated using two-tailed unpaired t-test between biological replicates. n.s. = not significant, ** $p<0.01$, *** $p < 0.001$.

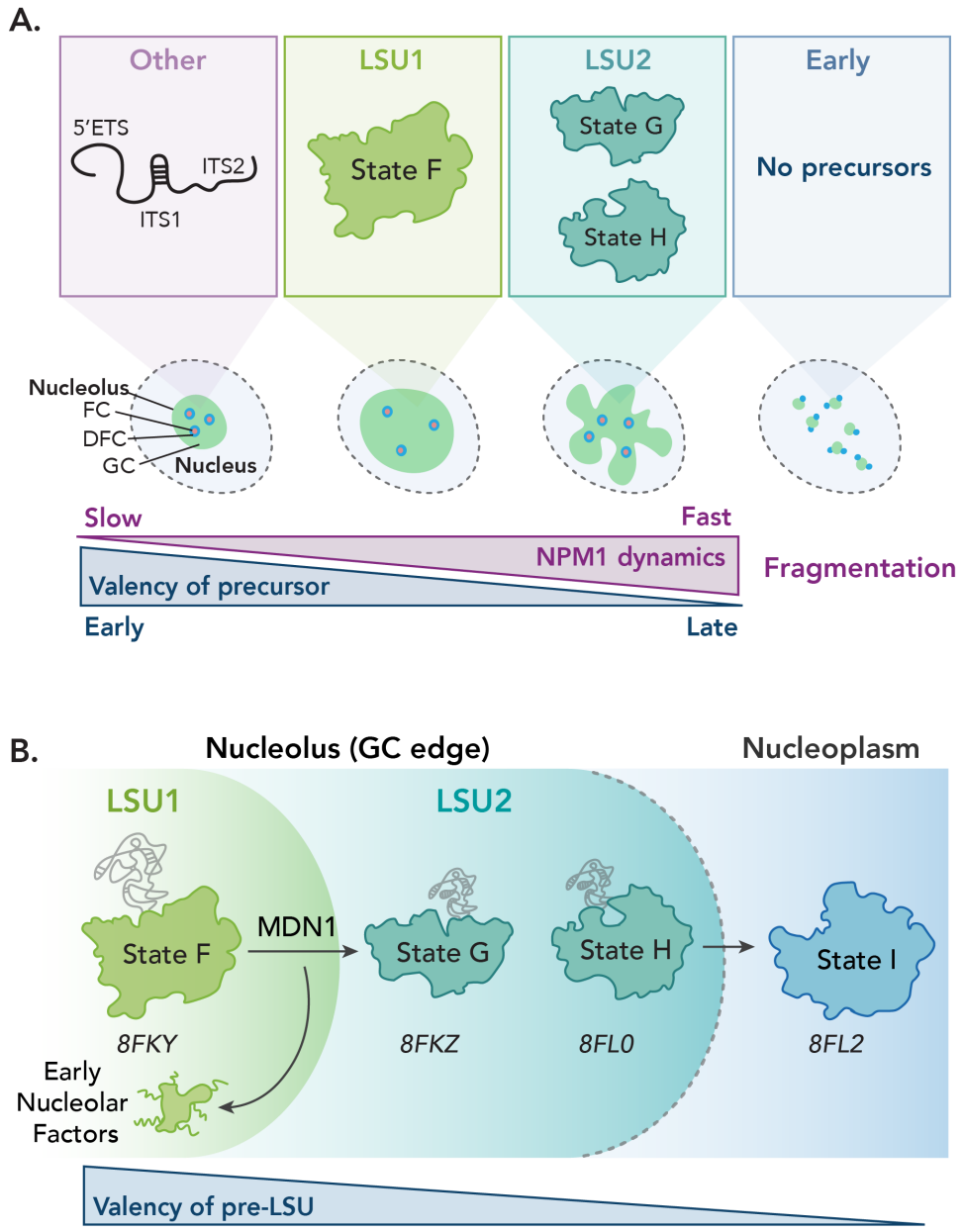

Figure 7: Model for how ribosome assembly impacts nucleolar biophysical features. (A) Model for how ribosome intermediates determine nucleolar biophysical properties. (B) Model for pre-LSU export from the nucleolus. Uncompacted IDRs and rRNA indicated graphically.

Materials and Methods

Key resources table

Reagent or resource	Designation	Source or reference	Identifiers	Additional information
Cell line (human)	HeLa cell line with inducible Cas9 (cTT20.11)	Gift from Kara L. McKinley and Iain Cheeseman (McKinley and Cheeseman, 2017)	N/A	Parent cell line used for NPM1-tagged reporter cells
Cell line (human)	Lenti-X HEK 293T cells	Takara Biosciences	Cat# 632180	For lentivirus production.
Cell line (human)	NPM1-mNeonGreen HeLa	This paper	N/A	Tagged at endogenous locus.
Cell line (human)	NPM1-mScarlet HeLa	This paper	N/A	Tagged at endogenous locus.
Cell line (human)	$NPM1^{WT}$-mScarlet HeLa	This paper	N/A	
Cell line (human)	$NPM1^{mA2}$-mScarlet HeLa	This paper	N/A	
Cell line (human)	$NPM1^{mB1}$-mScarlet HeLa	This paper	N/A	
Cell line (human)	$NPM1^{mA3}$-mScarlet HeLa	This paper	N/A	
Cell line (human)	$NPM1^{mB2}$-mScarlet HeLa	This paper	N/A	
Cell line (human)	NPM1 knockout HeLa	This paper	N/A	
Cell line (human)	$NPM1^{WT}$-mScarlet in NPM1 knockout HeLa	This paper	N/A	
Cell line (human)	$NPM1^{mA3}$-mScarlet in NPM1 knockout HeLa	This paper	N/A	
Cell line (human)	$NPM1^{mB2}$-mScarlet in NPM1 knockout HeLa	This paper	N/A	
Construct/Plasmid	GFP-NPM WT	Gift from Xin Wang, (Wang. W et al., 2005)	Addgene # 17578	Used to obtain sequence of NPM1-WT.
Construct/Plasmid	pX330	Gift from Feng Zhang	Addgene # 42230	
Construct/Plasmid	pKLM73	Gift from Kara L. McKinley		Donor plasmid with C-terminal mNeonGreen and puromycin resistance cassette

Construct/Plasmid	pKLM110	Gift from Kara L. McKinley		Donor plasmid with C-terminal mScarlet and puromycin resistance cassette
Construct/Plasmid	pKLM79	Gift from Kara L. McKinley		Lentivirus transfer plasmid with C-terminal mScarlet Fusion tag. SFFV promoter. Used for NPM1 mutant constructs.
Construct/Plasmid	NPM1-mNeonGreen-Puro^{R} donor plasmid	This paper		
Construct/Plasmid	NPM1-mScarlet-Puro^{R} donor plasmid	This paper		
Construct/Plasmid	pX330-NPM1 sgRNA	This paper		Targeting sequence: GCCAGAGATCTTGAATAGCC
Construct/Plasmid	SFFV-NPM1^{WT}-mScarlet	This paper		
Construct/Plasmid	SFFV-NPM1^{mA2}-mScarlet	This paper		
Construct/Plasmid	SFFV-NPM1^{mB1}-mScarlet	This paper		
Construct/Plasmid	SFFV-NPM1^{mA3}-mScarlet	This paper		
Construct/Plasmid	SFFV-NPM1^{mB2}-mScarlet	This paper		
Software	μManager	Edelstein et al., 2014	Latest nightly build	https://micro-manager.org/
Software	Pycromanager	Pinkard, H. et al., 2021		https://github.com/micro-manager/pycro-manager/
Software	R	R Core Team, 2021	v. 4.1.1	https://www.r-project.org/
Software	Prism	GraphPad	v. 8.3.0	
Software	FIJI	Schindelin et al., 2012		https://imagej.net/software/fiji/
Software	CellProfiler	Stirling, D. R. et al., 2021	v.4.0.7	https://cellprofiler.org/
Oligonucleotide	5'ETS RNA FISH probe	Integrated DNA Technologies		Cy3-CGGAGGCCCAACCTCTCCGACGACAGGTCGCCAGAGGACAGCGTGTCAGC
Oligonucleotide	ITS1 RNA FISH probe	Integrated DNA Technologies		Cy3-CCTCGCCCTCCGGGCTCCGGGCTCCGTTAATGATC
Oligonucleotide	ITS2 RNA FISH probe	Integrated DNA Technologies		Cy3-CTGCGAGGGAACCCCCAGCCGCGCA

Oligonucleotide	SKIV2L2 ON-TARGETplus siRNA SMARTPool	Horizon Discovery	Cat # L-031902-02-0005	
Oligonucleotide	UPF1 ON-TARGETplus siRNA SMARTPool	Horizon Discovery	Cat # L-011763-00-0005	
Oligonucleotide	DDX54 ON-TARGETplus siRNA SMARTPool	Horizon Discovery	Cat # L-017128-01-0005	
Oligonucleotide	eIF4A3 ON-TARGETplus siRNA SMARTPool	Horizon Discovery	Cat # L-020762-00-0005	
Oligonucleotide	NSA2 ON-TARGETplus siRNA SMARTPool	Horizon Discovery	Cat # L-017043-01-0005	
Oligonucleotide	MDN1 ON-TARGETplus siRNA SMARTPool	Horizon Discovery	Cat # L-009786-00-0005	
Oligonucleotide	RPF2 ON-TARGETplus siRNA SMARTPool	Horizon Discovery	Cat # L-024715-01-0005	
Oligonucleotide	GNL2 ON-TARGETplus siRNA SMARTPool	Horizon Discovery	Cat # L-020392-01-0005	
Oligonucleotide	PHF5A ON-TARGETplus siRNA SMARTPool	Horizon Discovery	Cat # L-014987-01-0005	
Oligonucleotide	CNOT1 ON-TARGETplus siRNA SMARTPool	Horizon Discovery	Cat # L-015369-01-0005	
Antibody	α-tubulin Monoclonal antibody (DM1A)	Invitrogen	Cat # 62204	
Antibody	eIF4A3 polyclonal antibody (Rabbit)	Proteintech	Cat 3 17504-1-AP	
Antibody	UPF1 (D15G6) Rabbit mAb	Cell Signaling Technology	Cat # 12040	
Antibody	SKIV2L2 polyclonal antibody (Rabbit)	Novus Biologicals	Cat # NB100-1574	

Antibody	DDX54 polyclonal antibody (Rabbit)	Proteintech	Cat # 26894-1-AP	
Antibody	NOL1 Antibody	Novus Biologicals	Cat # NBP1-92192	
Antibody	GNL2 Antibody	Novus Biologicals	Cat # NBP1-81649	
Antibody	GLTSCR2 Polyclonal Antibody	Proteintech	Cat # 27353-1-AP	
Antibody	Goat anti-Mouse IgG (H+L) Cross-Absorbed Secondary Antibody, Alexa 647	Invitrogen	Cat # A-21235	
Antibody	Goat anti-Rabbit IgG (H+L) Cross-Absorbed Secondary Antibody, Alexa 647	Invitrogen	Cat # A-21245	
Antibody	Anti-mouse IgG, HRP-linked	Cell Signaling Technology	Cat # 7076S	
Antibody	Anti-Rabbit IgG (whole molecule)-Peroxidase antibody	Millipore	Cat # A0545-1ML	
Reagent	RFP-Trap Agarose	Chromotek	Cat # rta	
Chemical	Actinomycin D	Sigma	Cat # A1410-2MG	
Chemical	CX-5461	SelleckChem	Cat # S2684	
Chemical	Pladienlolide B	Tocris	Cat # 6070	
Chemical	Sodium Arsenite	Millipore	Cat # 7784-46-5	
Chemical	MG132	SelleckChem	Cat # S2619	
Chemical	SMG1i	Gift from Rosalind Franklin University of Medicine and Science and Cystic Fibrosis Foundation		
Chemical	Hoechst 22242	ThermoFisher	Cat # H3570	
Chemical/Reagent	Lipofectamine LTX	ThermoFisher	Cat # 15338030	
Chemical/Reagent	Lipofectamine 2000	ThermoFisher	Cat # 11668027	

Chemical/Reagent	Lipofectamine RNAiMAX	ThermoFisher	Cat # 13778075	
Chemical/Reagent	SE Cell Line 4D-Nucleofector X Kit	Lonza	Cat # V4XC-1032	
Chemical/Reagent	EnGen Spy Cas9 NLS	New England Biolabs	Cat # M0646T	

Cell culture

HeLa (cTT20.11[92], gift from Kara L. McKinley and Iain Cheeseman) and Lenti-X HEK293T cells (Takara Bio, used for lentivirus production) were cultured in DMEM (Gibco) supplemented with 10% tetracycline-free FBS (Gemini) and penicillin and streptomycin (Gibco) at 37°C with 5% CO_2 in a humidified incubator. Cells were maintained at passage number under 25 and routinely checked for mycoplasma. Cells were passaged using 0.05% Trypsin-EDTA (Gibco).

Endogenously-tagged cell line generation

Endogenously-tagged cell lines were generated using CRISPR-Cas9 homology directed repair. Guide RNAs targeting the last exon of NPM1 and FBL were designed using the Benchling CRISPR tool to maximize on-target and minimize off-target effects (targeting sequence: NPM1-GCCAGAGATCTTGAATAGCC; FBL-AACTGAAGTTCAGCGCTGTC). This sequence was inserted into pX330 (gift of Feng Zheng, Addgene #42230), which encodes both spCas9 and the sgRNA. Homology arms for genes of interest were ordered from IDT as gBlocks with PAM sequence for sgRNA mutated. Homology arms were cloned into pKLM73 for mNeonGreen and pKLM110 for mScarlet (gifts from Kara L. McKinley) using NEBuilder HiFi DNA Assembly (New England Biolabs). To generate knock-in lines, HeLa cells were seeded in a 6-well plate at $1x10^6$ cells per well. The following day, cells were transfected with 1 μg each of the pX330 and donor plasmids using Lipofectamine 2000 (ThermoFisher). After 72 hr, cells were passaged into 10 cm dishes and cells with integration were selected for using puromycin at 1 μg/mL. After sufficient cell death and outgrowth of resistant colonies, cells were passaged one additional time to recover and then fluorescently positive cells were sorted for single cells into a 96-well plate using a Sony SH800 cell sorter. Single-cell clones were checked for correct localization of tagged protein and confirmed by genotyping PCR. Briefly, gDNA was isolated from a confluence 12-well plate by rinsing once with PBS followed by addition of 0.5 mL genomic DNA lysis buffer (100 mM Tris pH 8, 5 mM EDTA, 200 mM NaCl, 0.2% SDS, 0.2 mg/mL proteinase K). Plates were incubated with lysis buffer at 37°C overnight. Lysed cells were transferred to an Eppendorf tube and DNA was precipitated using isopropanol followed by washing with 70% ethanol. Pellet was resuspended in TE buffer (1 mM EDTA pH 8, 10 mM Tris pH 8) and used as a template for amplification of insertion regions. Products were visualized for size differences by agarose gel and then gel purified and submitted for Sanger sequencing.

Knockout cell line generation

NPM1 was stably ablated from HeLa cells (cTT20.11) using CRISPR-Cas9 as follows. Gene Knockout Kit v2 against NPM1 from Synthego was used for guide RNAs. 180 pmol guides were complexed with 20 pmol EnGen Spy Cas9 NLS (New England Biolabs) for 10 min at room temperature. The assembled Cas9 RNP was nucleofected into 1.5 x 10^5 cells using Lonza 4D-Nucleofector X unit and SE Cell Line Kit following manufacterer's protocol. Polyclonal population was assessed for knockdown by western blot and then sorted into single cells using a SONY SH800. Single cell clones were assessed for knockdown by western blot against NPM1 and Sanger sequencing.

Microscopy

All live-cell and fixed-cell confocal imaging was carried out on a Nikon Ti-E inverted microscope equipped with a Yokogawa CSU-X high-speed confocal scanner unit and a pair of Andor iXon 512 × 512 EMCCD cameras. All components of the microscope were controlled by the open-source platform μManager[93]. The microscope stage was enclosed in a custom-built incubator that maintains preset temperature. Live-cell imaging was

performed at 37°C with 5% CO_2 and cells were equilibrated on the microscope for at least 30 min prior to imaging. Fixed-cell imaging was performed at room temperature. High-magnification images were obtained using a 100x 1.49 NA oil-immersion objective. HiT-FRAP and high-content images were acquired with a 40x 0.95 NA air objective. For HiT-FRAP, images for mNeonGreen cells and mScarlet cells were collected at 100x EM gain with a 50 ms and 100 ms exposure, respectively. Bleaching was performed with a 405 nm focused laser beam set at 10 mW power steered by a pair of galvo mirrors (Rapp UGA-40), which was controlled by the Projector Plugin in μManager.

HiT-FRAP acquisition

Automated FRAP experiments were performed using custom code and the Python library Pycromanager , which integrates hardware control with image processing via μManager. Image processing was performed using scikit-image[95]. Positions and wells for acquisition were defined using the μManager High Content Screening (HCS) Site Generator Plugin. Exposure length was predetermined for each cell line to avoid saturated pixels. HiT-FRAP acquisition proceeded as follows: at each field of view, a single image was acquired. Organelles of interest were then identified. Firstly, the background pixel threshold was determined using Otsu's method. Threshold values for nucleoli were determined using local thresholding, and regions larger than 1000 pixels were removed. Both thresholds were combined and then subjected to two rounds of erosion and dilation, followed by removal of objects smaller than 10 pixels to clear the background. To maximize throughput, further analysis and acquisition only continued if greater than 20 organelles were present in a field of view. Centroids for organelles were then determined to generate a bleach position list. We set a size threshold for bleached organelles of at least twice the area of the bleach spot to preferentially capture internal mixing rather than exchange with the nucleoplasm, although due to limitations in magnification and the fixed size of our bleach laser, whole-organelle bleaches could not be completely avoided. A random 50% of these positions were then chosen for bleaching, with the remainder kept as controls to account for acquisition photobleaching. Bleach locations were exported for every field of view to be used in post-analysis. Acquisition then started, followed by concurrent bleaching at designated organelle centroid positions. Length of acquisition was manually pre-determined to achieve recovery plateau. This process was iterated through multiple fields of view until 500 bleaches were acquired, after which the stage was moved to the next well and the sequence repeated.

To account for drift in the bleach laser position, automated recalibration was performed as follows: after every two fields of view, a single image was acquired. The image was thresholded to identify cells using the triangle algorithm, and a position closest to the center that did not have a foreground object (cell) was determined. The bleach laser was then targeted to this location and an image was taken of the exposure. The true bleach laser position was determined from this image by identifying the maximum intensity position in the image. To increase the speed of finding this location, a region of interest was used based upon the estimated location of the bleach laser. When the square of the distance between the intended target and the true bleach spot location was greater than an offset of 5, a full calibration of the laser was performed.

HiT-FRAP image analysis

Analysis of high-content FRAP data was performed using the same software used for acquisition. For each FRAP recovery time series, nucleoli were identified in frame 0 using the same thresholding procedure as used for acquisition. Bleach spots were then identified as follows: the bleach positions generated during acquisition (pointers) were linked to the bleach frame. To account for experimental offsets in bleach positions, true bleach locations were determined empirically. Briefly, it was manually determined that the minimum intensity post-reported bleach time occurred after four frames (bleach time offset). For each pointer position, the minimum intensity frame (bleach frame + bleach time offset) was subtracted from the bleach frame and smoothed to remove background noise. Otsu global thresholding was then applied to identify bright spots (detected bleach spots). After two rounds of erosion and dilation to minimize background noise, the centroids of the closest detected bleach spots to each original pointer position were used as the true bleach location. These true bleach coordinates were then linked to the corresponding organelle. Bleach spots that fall outside of a

nucleolus, bleach the same nucleolus, overlap, or are too far away from the original pointer position (>20 pixels in any direction) were filtered. Bleach spot masks were then generated by subjecting the true bleach coordinates to three rounds of dilation.

Using these bleach spot masks, FRAP curves were determined as follows: to monitor photobleaching due to acquisition, control spot masks were generated by identifying centroids of unbleached organelles and submitting these to three rounds of dilation. Raw intensities for the bleach and control spots were calculated over the time course. Background was determined for each frame by generating a binary image of regions with a pixel intensity of less than 300, removing regions smaller than 50 pixels. The mean intensity of the largest area was used as background and subtracted from all measured intensities. A photobleaching factor was then determined for control spots and calculated as the intensity ratio between the control spot at every time point as compared to intensity at $t = 0$. The mean of this ratio across all control spots was then used as a correction factor for bleach spot intensities. These intensities were then normalized to the pre-bleach intensity and minimium intensity (0 to 1) to generate final intensities for fitting. These intensities were then fit to several FRAP models (single exponential, double exponential, soumpasis, and ellenberg), although single exponential fittings were used in all subsequent analyses. Curves were filtered out if they had less than 5 frames prior to bleach (to avoid poor determination of pre-bleach intensity), imaged for less than 100 frames post bleach for mNeonGreen or 50 frames for mScarlet (to ensure adequate recovery), if the mobile fraction was less than 0 or greater than 1.05, and if $R^2 < 0.7$. Parameters from the fitted curve are then exported (initial slope, mobile fraction, and $t_{1/2}$).

Organelle features were determined as follows: for each bleached nucleolus, the following organelle features available in scikit-image were calculated: area, mean intensity, circularity, eccentricity, solidity, minimum intensity, maximum intensity, perimeter, hu moments (2nd, 3rd, and 4th), intensity percentiles (1st, 5th, 95th, and 99th), median intensity, the standard deviation of intensities, intensity kurtosis, and intensity skew.

Dynamics screen phenotype analysis

Gene depletions with high cell death were removed manually from all subsequent analysis (DDX19B, DDX19A+DDX19B, DDX39A+DDX39B, and SNRNP200, CRNKL2, CWC22, EFTUD3, eS4, eS6, PRPF8, SNW1). Dynamics features (mobile fraction and $t_{1/2}$) were normalized using the median and median absolute deviation for all non-targeting siRNA controls in the same plate to account for plate-to-plate variation (robust z-score). Medians of robust z-scores were computed and used in final hit calling. p-values were calculated using the Kolmogorov-Smirnov test as compared to a randomly chosen subset (10%) of non-targeting control wells. FDR was determined using the Benjamini-Hochberg procedure. As indicated in the figure legends, an FDR threshold of 0.05 was used for defining significance. Thresholds for z-scores were set as indicated in figure legends.

Principal component analysis for multidimensional analysis

Phenotype scores were calculated and incorporate the -ln(p-value) (determined by Kolmogorov-Smirnov test) and effect size as compared to a subset (randomly selected 10%) of non-targeting control wells in the same plate to account for plate-to-plate variation. The remainder of non-targeting controls were treated as experimental samples to test the robustness of the scoring method. Phenotype scores were scaled from 0 to 1 prior to further analysis. PCA was performed using the prcomp R package. The R packages ggplot2[96], ggfortify[97], and ggrepel[98] were used to generate figures and are available through CRAN. Hits were manually called by separation from NT control cluster.

Hierarchical clustering to identify phenotype clusters

Robust z-scores for hits were used in hierarchical clustering using the pheatmap R package[99] by Ward's minimu variance method, variant D2. The resulting dendrogram was split into subtrees until clusters represented similar overall trends, generating five phenotypic clusters shown in Fig. S4B.

Cloning for mutant NPM1 lentivirus constructs
All constructs were cloned into the lentiviral transfer plasmid pKLM79 (gift of Kara L. McKinley), which contains a C-terminal mScarlet fusion tag. The wild-type sequence of NPM1 was cloned from GFP-NPM WT (gift from Xin Wang, Addgene plasmid # 17578). Mutant NPM1 plasmids were constructed by ordering mutated regions as gBlocks from IDT with overhangs complementary to proximal regions. Proximal regions were then amplified from the wild-type construct to generate fragments with appropriate overhangs for assembly by NEBuilder HiFi DNA Assembly (New England Biolabs) into pKLM79 (cut with MluI and SpeI, New England Biolabs).

Lentivirus transduction
Lentiviral particles were packaged by transfecting Lenti-X 293T cells with transfer construct of interest and PSP and VSVG helper plasmids using Lipofectamine LTX (Thermo Fisher) reagent. Media was changed 18 hr later and virus was harvested 72hrs after transfection. Virus was cleared by passing through a 0.45 μm PVDF filter. 200 μL viral supernatant was used to transduce a 6-well plate of HeLa cells by spinfection. Briefly, cells were seeded in suspension at 250,000 cells per well in the presence of viral supernatant and polybrene (Sigma-Aldrich) at a final concentration of 10 μg/mL. Cells were spun at 1000 x g for 45 min at 37°C and allowed to recover overnight. Media was replaced the following day and transduction was allowed to proceed for 48 hr until passage. Cells were passaged for at least two passages to eliminate cells that exhibited toxic levels of expression. Fluorescent cells were sorted using a Sony SH800 cell sorter gated to select the top 40% of expressing cells. Polyclonal populations were used for all experiments.

siRNAs
For the primary RNA helicase and secondary screen, candidate libraries of ON-TARGETplus SMARTPool siRNAs (4 guides per gene) were ordered in arrayed format from Horizon Discovery. Non-targeting siRNA pools were interspersed randomly throughout the plate at a ratio of 1:6 to on-target pools. For depooled validation, deconvoluted guide pools (single guides) were ordered in an arrayed format for select hits. Single non-targeting guides were interspersed randomly throughout the plate at a ratio of 1:6. For knockdown of single genes, ON-TARGETplus siRNA pooled guides were ordered from Horizon Discovery (see Key Resources Table).

siRNA transfections
For screens and depooled validation experiments, siRNAs were reverse transfected at a final concentration of 5nM using Lipofectamine RNAiMAX reagent (Life Technologies). Briefly, siRNA:lipid mixes were pipetted into wells of a 384-well glass bottom dishes (Matriplate; Brooks). After a 15 min incubation, cells were seeded at 900 cells per well. Knockdown was allowed to proceed for 72 hr before imaging. For validation experiments (RNA FISH, IF, and single gene knockdowns), pooled guide RNAs were reverse transfected at a final concentration of 25 nM into 96-well glass-bottom imaging plates (Matriplate; Brooks), with cells seeded at a density of 8000 cells per well. For qPCR and westerns, cells were reverse transfected with pooled guide RNAs at a final concentration of 25 nM into 24-well tissue culture dishes (Corning) and cells were plated at 24,000 cells per well.

Drug treatments
For all drug treatments, cells were seeded at 50,000 cells per well into 96-well glass bottom imaging dishes (Matriplate; Brooks) 24 hr prior to experiments. For ATP depletion, cells were washed twice in DMEM without glucose (Gibco) and then incubated for 10 min with 10 mM sodium azide and 6mM 2-deoxyglucose diluted in DMEM without glucose supplemented with 10% tetracycline free FBS (Gemini). For sodium arsenite, cells were treated with 200 μm sodium arsenite diluted in culture media for 1 hr prior to imaging. For MG132, cells were treated with 10 μm MG132 diluted in culture media for 1 hr prior to imaging. For Pol I inhibitors, cells were treated with 0.04 μg/mL actinomycin D (Sigma) or 500 nM CX5461 (SelleckChem) diluted in culture media for 2 hr. For pladienolide B treatment, cells were treated with 10 nM PladB (Tocris, initially diluted in DMSO) diluted in culture media for 24 hr. For SMG1i treatment, cells were treated with 300 nM SMG1i (initially diluted in DMSO) diluted in culture media for 24 hr. All drug treatments were compared to cells treated with

equal volumes of vehicle. For all imaging experiments, cells were transferred to heated and equilibrated microscope at least 30 min prior to imaging.

RNA fluorescent in situ hybridization (RNA FISH)

RNA FISH was performed in a 96-well plate format (see siRNA transfections). After knockdown or drug treatment, cells were fixed in 4% Paraformaldehyde in PBS at 37°C for 10 min. Cells were then permeabilized by incubation with ice-cold methanol at -20°C for 10 min. Cells were incubated with 1 M Tris pH 8 for approximately 10 min. 5' Cy5 labeled DNA probes (see Supplementary Table 1) were ordered from IDT and resuspended at 1 μg/mL in water. Stock probes were diluted 1:1000 in RNA FISH hybridization buffer preheated to 42°C (15% deionized formamide, 10% dextran sulfate, 2x SSC from Ambion, 0.02% BSA, 0.2 mg/mL Baker's yeast tRNA from Ambion). Plate was placed in plastic bag with wet paper towels and incubated at 42°C for 1 hr. Cells were washed with 2x SSC three times at room temperature, followed by incubation with Hoechst 33342 DNA dye diluted at 1:1000 in 2x SSC for 10 min at room temperature. Cells were washed a final three times with 2x SSC and then imaged.

Immunofluorescence (IF)

Immunofluorescence was performed in 96-well plate format (see siRNA transfections). After knockdown or drug treatment, cells were fixed in 4% Paraformaldehyde in PBS at 37°C for 10 min. Cells were then permeabilized by incubation with ice-cold methanol at -20°C for 10 min. Fixed cells were blocked in 3% BSA in PBST (PBS from Gibco supplemented with 0.1% Tween-20) for at least 1 hr, followed by incubation overnight with primary antibodies diluted at 1:500 in antibody dilution buffer (3% BSA, PBST, 0.02% sodium azide). The following day, cells were washed three times with PBST followed by incubation for 1-2 hr at room temperature with appropriate secondary antibody conjugated to Alexa 647 (ThermoFisher) diluted at 1:1000 in antibody dilution buffer. Cells were then washed three times with PBST and incubated with Hoechst 33342 DNA dye (Invitrogen) diluted at 1:1000 for 10 min at room temperature. Cells were washed a final three times with PBST and then imaged.

NPM1 Immunoprecipitation for western blotting and qPCR

15 cm dishes of NPM1-mScarlet expressing cells were seeded 24-48 hr prior to experiment such that cells were 70% confluent at time of harvest. Cells were washed once with ice cold PBS and then scraped into 1 mL ice cold lysis buffer (Pierce IP Lysis Buffer, ThermoFisher) supplemented with 0.5 mM TCEP and protease inhibitors (cOmplete Mini Tablets, Roche). Cells were sonicated at 30% power for 20 sec followed by ~2 min on ice, three times in total. Cells were then spun at 16,000 x g at 4°C for 10 min to remove cell debris. An aliquot of lysate was removed for input samples, and then the remainder was split into two parts and each bound to 25 μL RFP-Trap resin (slurry, which was first washed with 1 mL of lysis buffer). Samples were bound for 1 hr at 4°C while rotating. Resin was washed twice with lysis buffer and then 4 times with wash buffer (25 mM Tris pH 7.4, 150 mM NaCl, 1mM EDTA, 0.05% NP-40, 0.5 mM TCEP). Samples for western blot were then eluted directly in 50 μL sample buffer (2% SDS, 10 mM EDTA, 10% glycerol, 0.1% bromophenol blue, 50 mM Tris, pH 7.4, 100 mM DTT). Samples for qPCR were eluted directly into 100 μL TRIzol reagent (ThermoFisher). Sample preparation then continued as described below.

RT-qPCR

Cells were transfected in 24-well format, see siRNA transfection protocol above. After 72 hr of gene knockdown, cells were rinsed twice with ice-cold PBS (Gibco) and then scraped into 200 μL TRIzol Reagent (Invitrogen) and lysed by pipetting. Lysed cells were incubated for 5 min at room temperature. 40 μL chloroform was added and tubes were mixed by inversion followed by incubation for 2 minutes at room temperature. Samples were centrifuged for 15 min at 12,000 x g at 4°C. The aqueous phase was transferred to a new tube. RNA was extracted using Zymo RNA Clean and Concentrator kit according to manufacturer's protocol. RNA was eluted in 15 μL RNase-free water (Ambion). cDNA was generated from 1 μg total RNA using iScript cDNA Synthesis Master Mix (Bio-Rad). cDNA was then diluted 1:20 for rRNA intermediates and 1:100 for mature rRNAs. RT-qPCR was performed using SYBR Green PCR Master Mix (Applied Bioystems) according to

manufacturer's protocol with a Bio-Rad CFX 96 Real Time thermal cycler. Reactions were run in technical triplicate and GAPDH was used as a housekeeping gene with the following primers:
GAPDH-F (5'-GTCTCCTCTGACTTCAACAGCG-3')
GAPDH-R (5'-ACCACCCTGTTGCTGTAGCCAA-3')
Primers used to amplify rRNA regions were as follows:
47S-F (5'-GAACGGTGGTGTGTCGTT-3')
47S-R (5'-GCGTCTCGTCTCGTCTCACT-3')
18S_5'-F (5'-GCCGCGCTCTACCTTACCTACCT-3')
18S_5'-R (5'-CAGACATGCATGGCTTAATCTTTG-3')
18S_3'-F (5'-AGTCGTAACAAGGTTTCCGTAGGT-3')
18S_3'-R (5'-CCTCCGGGCTCCGTTAAT-3')
5.8S_5'-F (5'-TACGACTCTTAGCGGTGGATCA-3')
5.8S_5'-R (5'-TCACATTAATTCTCGCAGCTAGCT-3')
5.8S_3'-F (5'-GAATTGCAGGACACATTGATCATC-3')
5.8S_3'-R (5'-GGCAAGCGACGCTCAGA-3')
18S-F (5'-CTGGATACCGCAGCTAGGAA-3')
18S-R (5'-GAATTTCACCTCTAGCGGCG-3')
5.8S-F (5'-ACTCGGCTCGTGCGTC -3')
5.8S-R (5'-GCGACGCTCAGACAGG-3')
28S-F (5'-CGGCGGGAGTAACTATGACT-3')
28S-R (5'-GCTGTGGTTTCGCTGGATAG-5')
Primers used for assessing gene depletions were as follows (designed using IDT PrimeTime):
MDN1 F: (5'-TTCGAGCACATTAAACAAGGC-3')
MDN1 R: (5'-CCTCCTCTTCCTGATCTTTGC-3')
NOG2 F: (5'-CCAATGAGAGCCACTTGT-3')
NOG2 R: (5'-GATGGATTTGACCCTCACC-3')
PHF5A F: (5'- ATTGTAAGGAGTCACCATCC-3')
PHF5A R: (5'-GCGTTCATAGAAGAGGTCTGTC-3')
CNOT1 F: (5'-CTGTCATACTGTTGCCACTGAT-3')
CNOT1 R: (5'-CTCATACTCCCAACCTCTG-3')
NSA2 F: (5'-TGAGACCCGAAAATTGAGAGC-3')
NSA2 R: (5'-GGTAATCCAAACGGTATCCATAGC-3')
RPF2 F: (5'-GTATGTTCTCACTTCACTGC-3')
RPF2 R: (5'-TCCCATCTCTTCCAATTCAATCC-3')

Western blotting

Cells were washed twice with ice-cold PBS and then scraped into RIPA buffer (ThermoFisher) supplemented with protease inhibitors (cOmplete Mini Tablets, Roche). Cells were lysed by with a probe sonicator at 20% power in two 30-sec intervals on ice. Lysates were normalized by OD_{260} and denatured in sample buffer and boiled for 5 min at 95°C. Samples were run on a 4-20% Mini-PROTEAN TGX precast gel (Bio-Rad) and then transferred to nitrocellulose using a Bio-Rad TransBlot Turbo system. Membranes were blocked in 3% w/v BSA in TBST (50 mM Tris pH 8, 150 mM NaCl, 0.1% TWEEN-20) for 30 min and then incubated with primary antibodies overnight diluted at 1:1000 in antibody dilution buffer (3% BSA in TBST with 0.02% sodium azide). Membranes were washed three times in TBST and then incubated in 1:10,000 secondary antibody diluted in 3% BSA in TBST for 1-2 hr. Membranes were again washed three times in TBST and then incubated in SuperSignal West Pico Plus ECL substrate (ThermoFisher) and imaged on a Bio-Rad ChemiDOC MP Imaging system.

Quantification of nucleolar RNA FISH and IF

Fixed-cell images were analyzed using custom pipelines developed in CellProfiler[100] (v.4.0.7). Briefly, for nucleolar RNA FISH, nucleoli were segmented using the NPM1-tagged channel using adaptive Otsu thresholding. There is a higher nucleoplasmic signal for FISH samples, and therefore, three threshold classes were used and the bottom two were classified as background. The object diameter range was set to 10-300 pixels, and objects outside this range were discarded. Nucleoli that touch the border of the image were discarded. Identified nucleoli were shrunk but 1 pixel to eliminate impacts of edge effects on intensity measurements. Intensity of identified nucleoli objects were measured for both the unscaled NPM1-tagged channel and the stained channel. For IF, the same pipeline was used, but nucleoli were thresholded using two class thresholding. A custom Python script was used for post-processing of CellProfiler data to bin images by field of view and experimental condition. In addition, nucleoli that had an NPM1 intensity level of less than 0.01 were eliminated to omit fields of view with no cells, which resulted in inappropriate identification of background noise.

Partition coefficient calculations

Partition coefficients were determined manually by quantifying relative nucleolar (I^{dense}) and nucleoplasmic (I^{dilute}) NPM1 intensities from pre-bleach (time point 0) images acquired by HiT-FRAP, as follows: Nucleolar signal was determined by measuring the average intensity of a 10 x 10 pixel box in the most intense region of nucleolar signal (5 x 5 pixels were used when nucleoli were small). Nucleoplasmic signal was determined by measuring the average intensity of a 10 x 10 pixel box that was manually chosen in the same cell as the measured nucleolus. Background was determined by averaging the average intensity across 5 randomly chosen 10 x 10 pixel locations. Background was subtracted, and then the ratio of nucleolar to nucleoplasmic signals were calculated to determine partition coefficient ($K = I^{dense}/I^{dilute}$, where K = partition coefficient).

RNA Helicase phylogenetic analysis

Full-length, reference protein sequences for indicated DEAD-box proteins were retrieved from NCBI and aligned using MUSCLE[101]. A maximum-likelihood tree was constructed using MEGA[102] using default options and the JTT model.

Statistical analysis

Software used for statistical analysis of screen-related data is listed in subsection of methods above. Otherwise, all other statistical tests were performed in Prism 8 as indicated in figure legends.

References

1. Shin, Y. & Brangwynne, C. P. Liquid phase condensation in cell physiology and disease. *Science* **357**, (2017).
2. Banani, S. F., Lee, H. O., Hyman, A. A. & Rosen, M. K. Biomolecular condensates: organizers of cellular biochemistry. *Nat Rev Mol Cell Biol* **18**, 285–298 (2017).
3. Lyon, A. S., Peeples, W. B. & Rosen, M. K. A framework for understanding the functions of biomolecular condensates across scales. *Nat Rev Mol Cell Biol* **22**, 215–235 (2021).
4. Alberti, S. & Hyman, A. A. Biomolecular condensates at the nexus of cellular stress, protein aggregation disease and ageing. *Nat Rev Mol Cell Biol* **22**, 196–213 (2021).
5. Mittag, T. & Pappu, R. V. A conceptual framework for understanding phase separation and addressing open questions and challenges. *Molecular Cell* **82**, 2201–2214 (2022).
6. Wang, Z., Lou, J. & Zhang, H. Essence determines phenomenon: Assaying the material properties of biological condensates. *Journal of Biological Chemistry* **298**, 101782 (2022).
7. Alshareedah, I., Moosa, M. M., Pham, M., Potoyan, D. A. & Banerjee, P. R. Programmable viscoelasticity in protein-RNA condensates with disordered sticker-spacer polypeptides. *Nat Commun* **12**, 6620 (2021).
8. Boeynaems, S. *et al.* Spontaneous driving forces give rise to protein−RNA condensates with coexisting phases and complex material properties. *Proceedings of the National Academy of Sciences* **116**, 7889–7898 (2019).
9. Wang, J. *et al.* A Molecular Grammar Governing the Driving Forces for Phase Separation of Prion-like RNA Binding Proteins. *Cell* **174**, 688-699.e16 (2018).
10. Donati, G., Montanaro, L. & Derenzini, M. Ribosome Biogenesis and Control of Cell Proliferation: p53 Is Not Alone. *Cancer Research* **72**, 1602–1607 (2012).

11. Lempiäinen, H. & Shore, D. Growth control and ribosome biogenesis. *Current Opinion in Cell Biology* **21**, 855–863 (2009).

12. Golomb, L., Volarevic, S. & Oren, M. p53 and ribosome biogenesis stress: The essentials. *FEBS Letters* **588**, 2571–2579 (2014).

13. Klinge, S. & Woolford, J. L. Ribosome assembly coming into focus. *Nat Rev Mol Cell Biol* **20**, 116–131 (2019).

14. Bohnsack, K. E. & Bohnsack, M. T. Uncovering the assembly pathway of human ribosomes and its emerging links to disease. *The EMBO Journal* **38**, e100278 (2019).

15. Parker, M. D. & Karbstein, K. Quality control ensures fidelity in ribosome assembly and cellular health. *Journal of Cell Biology* **222**, e202209115 (2023).

16. Broeck, A. V. & Klinge, S. Principles of human pre-60S biogenesis. 2023.03.14.532478 Preprint at https://doi.org/10.1101/2023.03.14.532478 (2023).

17. Singh, S., Vanden Broeck, A., Miller, L., Chaker-Margot, M. & Klinge, S. Nucleolar maturation of the human small subunit processome. *Science* **373**, eabj5338 (2021).

18. Krüger, T., Zentgraf, H. & Scheer, U. Intranucleolar sites of ribosome biogenesis defined by the localization of early binding ribosomal proteins. *Journal of Cell Biology* **177**, 573–578 (2007).

19. Lafontaine, D. L. J., Riback, J. A., Bascetin, R. & Brangwynne, C. P. The nucleolus as a multiphase liquid condensate. *Nat Rev Mol Cell Biol* **22**, 165–182 (2021).

20. Boisvert, F.-M., van Koningsbruggen, S., Navascués, J. & Lamond, A. I. The multifunctional nucleolus. *Nat Rev Mol Cell Biol* **8**, 574–585 (2007).

21. Riback, J. A. *et al.* Composition-dependent thermodynamics of intracellular phase separation. *Nature* **581**, 209–214 (2020).

22. Mitrea, D. M. *et al.* Nucleophosmin integrates within the nucleolus via multi-modal interactions with proteins displaying R-rich linear motifs and rRNA. *eLife* **5**, e13571 (2016).

23. Ferrolino, M. C., Mitrea, D. M., Michael, J. R. & Kriwacki, R. W. Compositional adaptability in NPM1-SURF6 scaffolding networks enabled by dynamic switching of phase separation mechanisms. *Nat Commun* **9**, 5064 (2018).

24. Brangwynne, C. P., Mitchison, T. J. & Hyman, A. A. Active liquid-like behavior of nucleoli determines their size and shape in Xenopus laevis oocytes. *Proceedings of the National Academy of Sciences* **108**, 4334–4339 (2011).

25. Feric, M. *et al.* Coexisting Liquid Phases Underlie Nucleolar Subcompartments. *Cell* **165**, 1686–1697 (2016).

26. Yao, R.-W. *et al.* Nascent Pre-rRNA Sorting via Phase Separation Drives the Assembly of Dense Fibrillar Components in the Human Nucleolus. *Molecular Cell* **76**, 767-783.e11 (2019).

27. LaPeruta, A. J., Micic, J. & Woolford Jr., J. L. Additional principles that govern the release of pre-ribosomes from the nucleolus into the nucleoplasm in yeast. *Nucleic Acids Research* gkac430 (2022) doi:10.1093/nar/gkac430.

28. Zhu, L. *et al.* Controlling the material properties and rRNA processing function of the nucleolus using light. *PNAS* **116**, 17330–17335 (2019).

29. Ogawa, L. M. *et al.* Increased numbers of nucleoli in a genome-wide RNAi screen reveal proteins that link the cell cycle to RNA polymerase I transcription. *Mol Biol Cell* **32**, 956–973 (2021).

30. Farley-Barnes, K. I. *et al.* Diverse Regulators of Human Ribosome Biogenesis Discovered by Changes in Nucleolar Number. *Cell Reports* **22**, 1923–1934 (2018).

31. Nicolas, E. *et al.* Involvement of human ribosomal proteins in nucleolar structure and p53-dependent nucleolar stress. *Nat Commun* **7**, 11390 (2016).

32. Taylor, N. O., Wei, M.-T., Stone, H. A. & Brangwynne, C. P. Quantifying Dynamics in Phase-Separated Condensates Using Fluorescence Recovery after Photobleaching. *Biophysical Journal* **117**, 1285–1300 (2019).

33. Negi, S. S. & Olson, M. O. J. Effects of interphase and mitotic phosphorylation on the mobility and location of nucleolar protein B23. *Journal of Cell Science* **119**, 3676–3685 (2006).

34. Frottin, F. *et al.* The nucleolus functions as a phase-separated protein quality control compartment. *Science* **365**, 342–347 (2019).

35. Moore, H. M. *et al.* Proteasome Activity Influences UV-Mediated Subnuclear Localization Changes of NPM. *PLOS ONE* **8**, e59096 (2013).

36. Latonen, L., Moore, H. M., Bai, B., Jäämaa, S. & Laiho, M. Proteasome inhibitors induce nucleolar aggregation of proteasome target proteins and polyadenylated RNA by altering ubiquitin availability. *Oncogene* **30**, 790–805 (2011).

37. Davis, Z. H. *et al.* Protein products of nonstop mRNA disrupt nucleolar homeostasis. *Cell Stress and Chaperones* **26**, 549–561 (2021).

38. Szaflarski, W. *et al.* Early rRNA processing is a stress-dependent regulatory event whose inhibition maintains nucleolar integrity. *Nucleic Acids Research* **50**, 1033–1051 (2022).

39. Hondele, M. *et al.* DEAD-box ATPases are global regulators of phase-separated organelles. *Nature* **573**, 144–148 (2019).

40. Linsenmeier, M. *et al.* Dynamic arrest and aging of biomolecular condensates are modulated by low-complexity domains, RNA and biochemical activity. *Nat Commun* **13**, 3030 (2022).

41. Overwijn, D. & Hondele, M. DEAD-box ATPases as regulators of biomolecular condensates and membrane-less organelles. *Trends in Biochemical Sciences* **48**, 244–258 (2023).

42. Mitterer, V. & Pertschy, B. RNA folding and functions of RNA helicases in ribosome biogenesis. *RNA Biol* **19**, 781–810.

43. Dembowski, J. A., Kuo, B. & Woolford, J. L. Has1 regulates consecutive maturation and processing steps for assembly of 60S ribosomal subunits. *Nucleic Acids Res* **41**, 7889–7904 (2013).

44. Burger, F., Daugeron, M.-C. & Linder, P. Dbp10p, a putative RNA helicase from Saccharomyces cerevisiae, is required for ribosome biogenesis. *Nucleic Acids Res* **28**, 2315–2323 (2000).

45. Choudhury, P., Kretschmer, J., Hackert, P., Bohnsack, K. E. & Bohnsack, M. T. The DExD box ATPase DDX55 is recruited to domain IV of the 28S ribosomal RNA by its C-terminal region. *RNA Biology* **18**, 1124–1135 (2021).

46. Chlon, T. M. *et al.* Germline DDX41 mutations cause ineffective hematopoiesis and myelodysplasia. *Cell Stem Cell* **28**, 1966-1981.e6 (2021).

47. Kanellis, D. C. *et al.* The exon-junction complex helicase eIF4A3 controls cell fate via coordinated regulation of ribosome biogenesis and translational output. *Sci Adv* **7**, eabf7561 (2021).

48. de Planell-Saguer, M., Schroeder, D. G., Rodicio, M. C., Cox, G. A. & Mourelatos, Z. Biochemical and genetic evidence for a role of IGHMBP2 in the translational machinery. *Human Molecular Genetics* **18**, 2115–2126 (2009).

49. Jalal, C., Uhlmann-Schiffler, H. & Stahl, H. Redundant role of DEAD box proteins p68 (Ddx5) and p72/p82 (Ddx17) in ribosome biogenesis and cell proliferation. *Nucleic Acids Res* **35**, 3590–3601 (2007).

50. Bohnsack, K. E., Yi, S., Venus, S., Jankowsky, E. & Bohnsack, M. T. Cellular functions of eukaryotic RNA helicases and their links to human diseases. *Nat Rev Mol Cell Biol* (2023) doi:10.1038/s41580-023-00628-5.

51. Szklarczyk, D. *et al.* The STRING database in 2023: protein-protein association networks and functional enrichment analyses for any sequenced genome of interest. *Nucleic Acids Res* **51**, D638–D646 (2023).

52. Dash, S. *et al.* rRNA transcription is integral to phase separation and maintenance of nucleolar structure. *PLOS Genetics* **19**, e1010854 (2023).

53. Neumüller, R. A. *et al.* Conserved Regulators of Nucleolar Size Revealed by Global Phenotypic Analyses. *Science Signaling* **6**, ra70–ra70 (2013).

54. Perry, R. P. & Kelley, D. E. Inhibition of RNA synthesis by actinomycin D: Characteristic dose-response of different RNA species. *Journal of Cellular Physiology* **76**, 127–139 (1970).

55. Perry, R. P. & Kelley, D. E. Persistent synthesis of 5S RNA when production of 28S and 18S ribosomal RNA is inhibited by low doses of actinomycin D. *Journal of Cellular Physiology* **72**, 235–245 (1968).

56. Drygin, D. *et al.* Targeting RNA polymerase I with an oral small molecule CX-5461 inhibits ribosomal RNA synthesis and solid tumor growth. *Cancer Res* **71**, 1418–1430 (2011).

57. Gallagher, J. E. G. *et al.* RNA polymerase I transcription and pre-rRNA processing are linked by specific SSU processome components. *Genes Dev.* **18**, 2506–2517 (2004).

58. Shav-Tal, Y. *et al.* Dynamic Sorting of Nuclear Components into Distinct Nucleolar Caps during Transcriptional Inhibition. *Mol Biol Cell* **16**, 2395–2413 (2005).

59. Riback, J. A. *et al.* Viscoelasticity and advective flow of RNA underlies nucleolar form and function. *Molecular Cell* **83**, 3095-3107.e9 (2023).

60. Kater, L. *et al.* Visualizing the Assembly Pathway of Nucleolar Pre-60S Ribosomes. *Cell* **171**, 1599-1610.e14 (2017).

61. Kawashima, S. A. *et al.* Potent, Reversible, and Specific Chemical Inhibitors of Eukaryotic Ribosome Biogenesis. *Cell* **167**, 512-524.e14 (2016).

62. Gamalinda, M. *et al.* A hierarchical model for assembly of eukaryotic 60S ribosomal subunit domains. *Genes Dev.* **28**, 198–210 (2014).

63. LaPeruta, A. J. *et al.* Yeast ribosome biogenesis factors Puf6 and Nog2 and ribosomal proteins uL2 and eL43 act in concert to facilitate the release of nascent large ribosomal subunits from the nucleolus. *Nucleic Acids Research* **51**, 11277–11290 (2023).

64. Biedka, S. *et al.* Hierarchical recruitment of ribosomal proteins and assembly factors remodels nucleolar pre-60S ribosomes. *Journal of Cell Biology* **217**, 2503–2518 (2018).

65. Gopalsamy, A. *et al.* Identification of pyrimidine derivatives as hSMG-1 inhibitors. *Bioorganic & Medicinal Chemistry Letters* **22**, 6636–6641 (2012).

66. Kotake, Y. *et al.* Splicing factor SF3b as a target of the antitumor natural product pladienolide. *Nat Chem Biol* **3**, 570–575 (2007).

67. White, M. R. *et al.* C9orf72 Poly(PR) Dipeptide Repeats Disturb Biomolecular Phase Separation and Disrupt Nucleolar Function. *Molecular Cell* **74**, 713-728.e6 (2019).

68. Dias, C. S., Araújo, N. A. M. & Telo da Gama, M. M. Dynamics of network fluids. *Advances in Colloid and Interface Science* **247**, 258–263 (2017).

69. Okuwaki, M., Saito, S., Hirawake-Mogi, H. & Nagata, K. The interaction between nucleophosmin/NPM1 and the large ribosomal subunit precursors contribute to maintaining the nucleolar structure. *Biochimica et Biophysica Acta (BBA) - Molecular Cell Research* **1868**, 118879 (2021).

70. Zorbas, C., Soenmez, A., Léger, J., De Vleeschouwer, C. & Lafontaine, D. L. Detecting material state changes in the nucleolus by label-free digital holographic microscopy. *EMBO reports* **25**, 2786–2811 (2024).

71. Sarkar, A. *et al.* Preribosomes escaping from the nucleus are caught during translation by cytoplasmic quality control. *Nat Struct Mol Biol* **24**, 1107–1115 (2017).

72. Rodríguez-Galán, O., García-Gómez, J. J., Kressler, D. & de la Cruz, J. Immature large ribosomal subunits containing the 7S pre-rRNA can engage in translation in Saccharomyces cerevisiae. *RNA Biology* **12**, 838–846 (2015).

73. Erdmann, P. S. *et al.* In situ cryo-electron tomography reveals gradient organization of ribosome biogenesis in intact nucleoli. *Nat Commun* **12**, 5364 (2021).

74. Farag, M. *et al.* Condensates formed by prion-like low-complexity domains have small-world network structures and interfaces defined by expanded conformations. *Nat Commun* **13**, 7722 (2022).

75. Folkmann, A. W., Putnam, A., Lee, C. F. & Seydoux, G. Regulation of biomolecular condensates by interfacial protein clusters. *Science* **373**, 1218–1224 (2021).

76. Zhang, Y. *et al.* Interface resistance of biomolecular condensates. *eLife* **12**, (2023).

77. Strom, A. R. *et al.* Condensate interfacial forces reposition DNA loci and probe chromatin viscoelasticity. *Cell* **0**, (2024).

78. Choi, C.-H., Lee, D. S. W., Sanders, D. W. & Brangwynne, C. P. Condensate interfaces can accelerate protein aggregation. *Biophysical Journal* **123**, 1404–1413 (2024).

79. Stenström, L. *et al.* Mapping the nucleolar proteome reveals a spatiotemporal organization related to intrinsic protein disorder. *Mol Syst Biol* **16**, e9469 (2020).

80. Darriere, T. *et al.* Upon heat stress processing of ribosomal RNA precursors into mature rRNAs is compromised after cleavage at primary P site in Arabidopsis thaliana. *RNA Biol* **19**, 719–734.

81. Berchtold, D., Battich, N. & Pelkmans, L. A Systems-Level Study Reveals Regulators of Membrane-less Organelles in Human Cells. *Molecular Cell* **72**, 1035-1049.e5 (2018).

82. Chhipi-Shrestha, J. K. *et al.* Splicing modulators elicit global translational repression by condensate-prone proteins translated from introns. *Cell Chemical Biology* **29**, 259-275.e10 (2022).

83. Jamar, N. H., Kritsiligkou, P. & Grant, C. M. Loss of mRNA surveillance pathways results in widespread protein aggregation. *Sci Rep* **8**, 3894 (2018).

84. Corman, A., Sirozh, O., Lafarga, V. & Fernandez-Capetillo, O. Targeting the nucleolus as a therapeutic strategy in human disease. *Trends in Biochemical Sciences* **48**, 274–287 (2023).

85. Nussbacher, J. K., Tabet, R., Yeo, G. W. & Lagier-Tourenne, C. Disruption of RNA Metabolism in Neurological Diseases and Emerging Therapeutic Interventions. *Neuron* **102**, 294–320 (2019).

86. Kwon, I. *et al.* Poly-dipeptides encoded by the C9orf72 repeats bind nucleoli, impede RNA biogenesis, and kill cells. *Science* **345**, 1139–1145 (2014).

87. Suzuki, H., Shibagaki, Y., Hattori, S. & Matsuoka, M. The proline–arginine repeat protein linked to C9-ALS/FTD causes neuronal toxicity by inhibiting the DEAD-box RNA helicase-mediated ribosome biogenesis. *Cell Death Dis* **9**, 1–16 (2018).

88. Tao, Z. *et al.* Nucleolar stress and impaired stress granule formation contribute to C9orf72 RAN translation-induced cytotoxicity. *Human Molecular Genetics* **24**, 2426–2441 (2015).

89. Mizielinska, S. *et al.* Bidirectional nucleolar dysfunction in C9orf72 frontotemporal lobar degeneration. *Acta Neuropathologica Communications* **5**, 29 (2017).

90. Sanders, D. W. *et al.* Competing Protein-RNA Interaction Networks Control Multiphase Intracellular Organization. *Cell* **181**, 306-324.e28 (2020).

91. Hiscox, J. A. RNA viruses: hijacking the dynamic nucleolus. *Nat Rev Microbiol* **5**, 119–127 (2007).

92. McKinley, K. L. & Cheeseman, I. M. Large-Scale Analysis of CRISPR/Cas9 Cell-Cycle Knockouts Reveals the Diversity of p53-Dependent Responses to Cell-Cycle Defects. *Dev Cell* **40**, 405-420.e2 (2017).

93. Edelstein, A. D. *et al.* Advanced methods of microscope control using μManager software. *J Biol Methods* **1**, e10 (2014).

94. Pinkard, H. *et al.* Pycro-Manager: open-source software for customized and reproducible microscope control. *Nat Methods* **18**, 226–228 (2021).

95. van der Walt, S. *et al.* scikit-image: image processing in Python. *PeerJ* **2**, e453 (2014).

96. Wickham, H. *Ggplot2: Elegant Graphics for Data Analysis*. (Springer-Verlag New York).

97. Tang Y, Horikoshi M, Li W. ggfortify: Unified Interface to Visualize Statistical Result of Popular R Packages. *The R Journal* **8**, 474--485 (2016).

98. Slowikowski, K. ggrepel: Automatically Position Non-Overlapping Text Labels with 'ggplot2'. (2023).

99. Kolde, R. pheatmap: Pretty Heatmaps. (2019).

100. Stirling, D. R. *et al.* CellProfiler 4: improvements in speed, utility and usability. *BMC Bioinformatics* **22**, 433 (2021).

101. Edgar, R. C. MUSCLE: multiple sequence alignment with high accuracy and high throughput. *Nucleic Acids Research* **32**, 1792–1797 (2004).

102. Stecher, G., Tamura, K. & Kumar, S. Molecular Evolutionary Genetics Analysis (MEGA) for macOS. *Mol Biol Evol* **37**, 1237–1239 (2020).